Trajectory Planning for Autonomous Driving Featuring Time-Varying Road Curvature and Adhesion Constraints

Yifan Gao, Wei Li, and Yu Hu, *Member, IEEE*

***Abstract*— Among the various driving situations, there are challenging road conditions where both the texture and curvature are variables over time (e.g., mountainous area). However, it is found that the characteristics of road texture and curvature have been respectively considered in some of the existing studies to determine the vehicle speed for trajectory planning, but the complementary effect of these two factors is still yet to be incorporated. This could lead to unsafe vehicle behaviour. This limitation has led us to develop a trajectory planning method that gives a systematic consideration of road conditions and leverages the complementary effect of road curvature and adhesion on the vehicle speed. It prioritises the trajectory safety through a preview of road constraints (i.e., waypoints, curvature and adhesion) in a look-ahead distance and the real-time computation of the vehicle speed that satisfies the constraints. In the experiment, our method was compared with the state-of-the-art techniques in a simulated mountainous driving environment, namely Model Predictive Control (MPC), Deep Reinforcement Learning (DRL) and Hybrid A*. The environment was built with abundant variation in road curvature and adhesion. The results showed that our approach was able to generate safe and comfort trajectories in both sharp turn and ice-covered driving scenarios, in which the vehicle successfully passed through the whole length of the global path without producing large deviations and exceeding lane boundaries. Whereas, the MPC, DRL and Hybrid A* approaches resulted in the vehicle exceeding lanes at some point with completeness levels of 77.72%, 75.31% and 79.53%, respectively.**

***Index Terms*— Road curvature, road adhesion, local trajectory planning, autonomous driving, varying road conditions.**

NOMENCLATURE

Abbreviations

MPC	model predictive control.
DRL	deep reinforcement learning.
PSO	particle swarm optimisation.
ANFIS	adaptive neuro-fuzzy inference system.
RDNN	recurrent deep neural network.
HD	high-definition.
AABB	axis-aligned bounding box.
IMU	inertial measurement unit.
OCBB	oriented capsule bounding box.
TRCA	time-varying road curvature and adhesion.
SGD	stochastic gradient descent.
CV	computer vision.

Variables

$s(t)$	vehicle longitudinal position at time t.
$s_{ld}(t)$	lead vehicle longitudinal position at time t.
$d(t)$	vehicle lateral position at time t.
$d_l(t)$	the position of the lane centre at time t.
$v_s(t)$	vehicle reference speed (longitudinal) at time t.
$\hat{v_s}(t)$	vehicle observed speed (longitudinal) at time t.
$v_d(t)$	vehicle reference speed (lateral) at time t.
$F_c^{max}(t)$	max centripetal force at time t.
$a_c^{max}(t)$	max centripetal acceleration at time t.
$a_c(t)$	reduced centripetal acceleration at time t.
$a_s(t)$	vehicle longitudinal acceleration at time t.
$a_d(t)$	vehicle lateral acceleration at time t.
$\rho(t)$	road curvature at time t.
$\eta(t)$	road adhesive at time t.

Constants

v_0	vehicle initial or predefined speed.
s_{sd}	safe distance from lead vehicle.
k	reduction rate to max centripetal acceleration.

Symbols

X_P	planned trajectory.
X_G	global path.
$P(x, y)$	vehicle current position in Cartesian space.
$P_t(x, y)$	vehicle target position in Cartesian space.
$P(s, d)$	vehicle current position in Frenet space.
$P(x_{\mathrm{clst}}, y_{\mathrm{clst}})$	waypoint closest to vehicle's current position.
m	mass of the vehicle.
g	gravitational acceleration.
l	length.
r	radius.
θ	tangent angle.
μ	arithmetic mean.
σ^2	variance.

Manuscript received 24 July 2023; revised 6 May 2024; accepted 12 June 2024. Date of publication 24 June 2024; date of current version 1 November 2024. This work was supported by the Key Research Project of Zhejiang Lab under Grant 2022PC0AC01. The Associate Editor for this article was J. W. Choi. *(Corresponding authors: Wei Li; Yu Hu.)*

Yifan Gao is with the Research Center for Frontier Fundamental Studies, Zhejiang Lab, Hangzhou 311121, China (e-mail: yfgao@zhejianglab.com).

Wei Li and Yu Hu are with the Research Center for Intelligent Computing Systems, Institute of Computing Technology, Chinese Academy of Sciences, Beijing 100190, China (e-mail: liwei@ict.ac.cn; huyu@ict.ac.cn).

Digital Object Identifier 10.1109/TITS.2024.3416289

I. INTRODUCTION

DRIVING autonomously is a long-standing goal in the field of artificial intelligence. This aspiration necessitates the vehicle being able to safely pass through different challenging road conditions [1]. The challenges consist of road geometry features such as serpentine and sharp bends that may prevent the autonomous driving system from reliably sustaining its current driving performance [2]. Another challenge is weather-informed road condition such as snow- and ice-covered road surfaces [3]. These challenges are significant contributors to traffic accidents. It was found that sharp bends were associated with increased number of traffic accidents. For example, in the district of Alapphuza, Kerala India, approximately 18.9% of all traffic accidents in 2019 were occurred at road segments with large curvatures. It was also counted that snowy weather-related accidents constituted 25.48% of all traffic accidents in China in 2018, where 4320 cases were occurred on snow- or ice-covered roads [4].

One of the main causes of accidents on sharp bends is that the driver does not reduce speed at the entrance to the bend, where the vehicle's trajectory curvature in real-time is less than the curvature of the road and overshoots the lane boundary [5]. The road's weather-informed texture also exerts a supplementary effect on the permissible speed of the vehicle in such case [6]. The texture varies the adhesion of the road, which determines both the frictional (centripetal) force and the permissible speed [7]. If the speed of the vehicle is not regulated as a function of curvature and texture on sharp bends and snow-covered sections, the vehicle could overshoot the lane boundary and cause accidents. A review of the existing literature finds that the time-varying curvature and texture features of road conditions have been considered respectively in some of the studies to determine the vehicle speed for trajectory planning, but the complementary effect of these two factors is still yet to be incorporated. Specifically, the determination of the vehicle speed in the existing methods can be described on three levels: 1) dynamic adaptation—with respect to predefined value/boundary, 2) dynamic adaptation—with respect to road curvature, and 3) dynamic adaptation—with respect to road adhesion.

At the level of 'dynamic adaptation—with respect to predefined value/boundary', the vehicle speed was either predefined based on the distances between waypoints divided by predefined time intervals, or formulated in terms of the minimum and maximum boundaries for trajectory optimisation. Chai et al. [8], [9] developed model predictive control (MPC)-based optimisers for the motion control of spacecraft re-entry vehicles, which form reference attitude trajectories that the re-entry vehicles can track. In their approaches, the minimum and maximum boundaries of the re-entry vehicle's angular velocity was appended as one of the constraints for an objective function to minimise the trajectory tracking errors. Liu et al. [10] presented a MPC-based approach for implementing optimal path following of autonomous vehicles, in which a constant vehicle velocity was assumed. Chai et al. [11] proposed a gradient-assisted particle swarm optimisation (PSO)-based motion generator for overtaking behaviour. In their approach, the maximum boundary of the vehicle's longitudinal velocity was added as one of the constraints for an objective function to minimise the overtaking time duration and ensure safety in the meantime.

At the level of 'dynamic adaptation—with respect to the road curvature', scholars have mathematically modelled the relationship between the vehicle speed and the road curvature and predicted the vehicle speed from the road curvature data. Cheng et al. [12] presented an adaptive neuro-fuzzy inference system (ANFIS) to approximate the quantitative relationship between the vehicle speed and the road curvature, which was built of an artificial neural network based on the Takagi-Sugeno theory of fuzzy inference. Chai et al. [13], [14], [15] proposed hierarchical deep learning-based frameworks for vehicle parking manoeuvre, which consist of an upper level trajectory generation layer and a lower level motion planning layer. In the trajectory generation layer, a recurrent deep neural network (RDNN) was trained for planning optimal parking maneuver trajectories. In the motion planning layer, a deep reinforcement learning (DRL) actor-critic network was adopted to learn the collision-free control policy from human demonstration data, in which the orientation angle of the vehicle which was affected by road curvature was used to regulate the reference speed.

At the level of 'dynamic adaptation—with respect to the road adhesion', researchers have mathematically modelled the relationship between the vehicle speed and the road adhesion and established a vehicle speed profile based on adhesion constraints. Pan et al. [16] used the quartic polynomial curve function to develop a trajectory generation algorithm for vehicle path following on snow-covered road. The algorithm is based on the Frenet coordinate system and takes into account the constraints of road adhesion for speed planning. Fu et al. [17] proposed a MPC-based trajectory planning framework for vehicle collision avoidance in highly constrained environments, which considers the road adhesion factor in the dynamic adaptation of the vehicle speed. Li et al. [18] presented a semantic-understanding trajectory planning framework, which consists of an upper level environment perception layer and a lower level trajectory sampling layer. The upper layer deals with the semantic perception of the environment and forms a collision-free space in real time. The lower layer uses the Hybrid A* search algorithm to sample an optimal trajectory based on the collision-free space provided by the upper layer, where the speed of the vehicle is constrained by the road adhesion to provide a solution that balances the safety-efficiency trade-off.

Another cause of accidents in challenging road conditions is limited planning horizon. In the discussed methods [12], [16], [18], the road information is not known *a priori*, where the positions of lane lines, sharp bends and texture variation are inferred using data obtained by the vehicle-mounted sensors and the planning horizon is limited by the range and quality of the sensors. In such case, the preview time might not be long enough for making smooth speed control at sharp bends and texture variation locations and accidents imply.

In conclusion, the discussed studies highlight the following two difficulties to be applied in challenging road conditions with curvature and texture as variables over time. Firstly, the

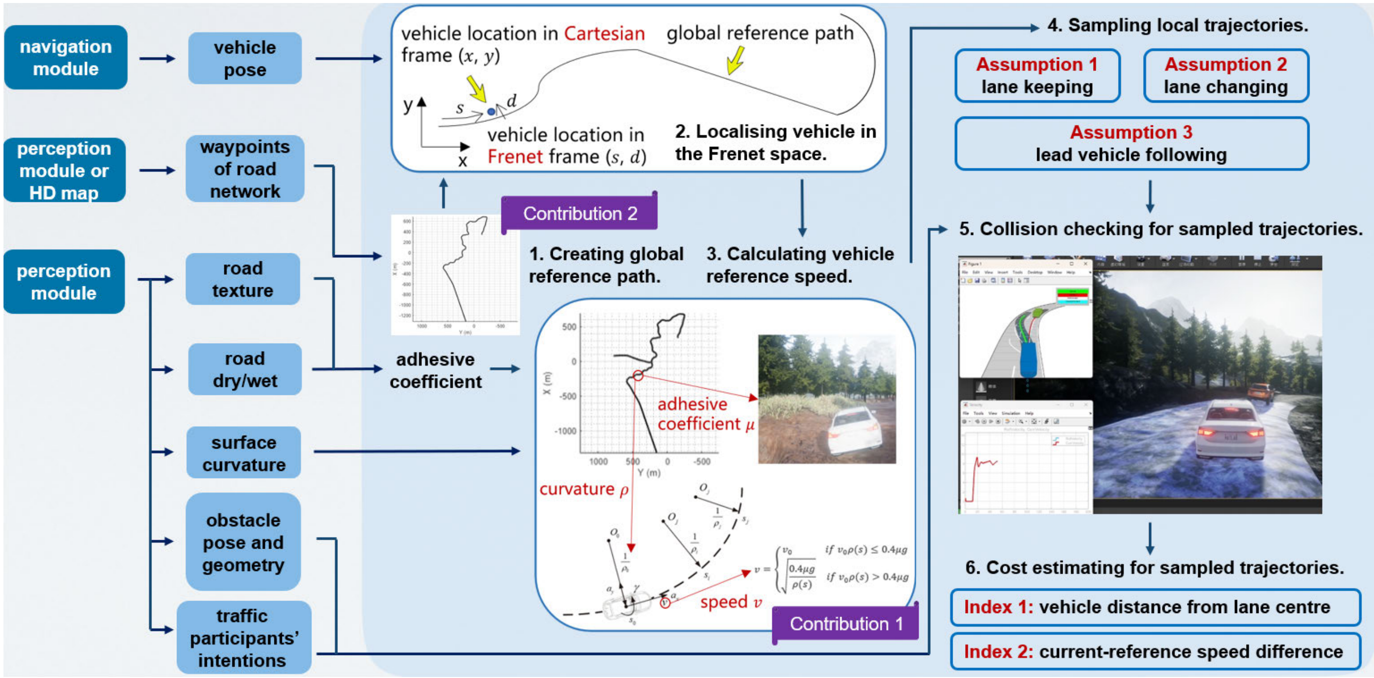

Fig. 1. Framework of the proposed approach.

speed of the vehicle is not regulated by both road curvature and texture features in the discussed methods. When encountered with road curves supplemented by weather influences, which is commonly seen in mountainous areas, the speed of the vehicle is not adequately modified and could cause accidents. Secondly, in some of the discussed methods, the planning horizon is limited by the range and quality of the vehicle-mounted sensors, leading to difficulties of sufficient preview time. Motivated by these considerations, this study presents a trajectory planning method that generates the vehicle speed in a way that ensures the safety of the manoeuvre in challenging road conditions. The main contributions of this paper can be attributed to the following three aspects:

1) The proposed method gives a systematic consideration of road conditions and leverages the complementary effect of road curvature and adhesion on the vehicle speed. It prioritises the trajectory safety through a preview of road constraints (i.e., waypoints, curvature, and adhesion) in a look-ahead distance and the real-time computation of the vehicle speed that satisfies the constraints. Specifically, the method is designed to mathematically model the relationship between vehicle speed, road curvature and adhesion, which has good adaptability for road section with time-varying curvature and adhesion features. This increases the safety of planned trajectories.
2) The proposed method achieves flexible trajectory planning horizon. This is enabled by a module of geometric interpolant, which creates a driving global path by performing a smooth interpolation of the waypoints representation of road network. The reference path provides *a priori* knowledge of lane lines and curves, in which the planning policy can have reference into the future and switch between non-myopic and myopic at a desirable distance. This feature allows sufficient preview time and increases the safety of planned trajectories.
3) The proposed method was tested through strategic design of experiments. The experimental environment consisted of abundant variation in road curvature and adhesion, in which the proposed method was tested in contrast with the state-of-the-art techniques from three aspects, including safety and comfort, structural similarity and efficiency. The proposed method is proved to be effective.

The rest of this paper is organized as follows. Section II presents the framework of the proposed trajectory planning method. Section III discusses the experiments and analytical results. Finally, Section IV concludes this study and discusses the future work.

II. PROPOSED METHOD

We achieved the research objectives by a preview of road constraints (i.e., waypoints, curvature, and adhesive coefficients) in a look-ahead distance and calculating the vehicle speed that satisfies the constraints. The framework overview and detailed steps of the proposed approach are presented in the following subsections.

A. Framework Overview

The framework of the proposed approach is depicted in Fig. 1. Specifically, the approach takes a 'vehicle localisation → trajectory generation → trajectory evaluation' planning scheme with the following steps as shown in Fig. 1:

1) Stage 1: Vehicle localisation.
    - Creating global reference path.
    - Localising vehicle in the Frenet space.
2) Stage 2: Trajectory generation.
    - Calculating vehicle reference speed.
    - Sampling local trajectories.

3) Stage 3: Trajectory evaluation.
   - Collision checking for sampled trajectories.
   - Cost estimating for sampled trajectories.

For vehicle localisation, the proposed approach interpolates points between the look-ahead waypoints of road network to form a continuous global reference path. Note that this study concentrates on the method of waypoints interpolation, where how to obtain the waypoints is not a focus of the research. Information of the waypoints ahead are assumed to be obtained from either the vehicle's on-board perception sensors or foreknown high-definition (HD) maps. By referring to the interpolated global path, the approach then converts the vehicle's position $P(x, y)$ as obtained in the Cartesian space to the Frenet coordinate $P(s, d)$. Compared with Cartesian, the Frenet space can describe a vehicle's position relative to the global path in a mathematically simpler and more intuitive manner [19]. The s and d values of the Frenet coordinate $P(s, d)$ respectively refer to a vehicle's run length along and offset distance from the global path. Note that this study concentrates on the method of Cartesian-Frenet conversion, where how to obtain the vehicle's position in Cartesian space is not a focus of the research. Such data are assumed to be obtained from the vehicle's on-board localisation sensors. The vehicle's localisation in the Frenet space is then provided to the trajectory generation level.

For trajectory generation, the proposed approach mathematically formulates the relationship between vehicle speed and time-varying road curvature and adhesive coefficients. The formulated relationship also considers a reasonable reduction to the maximal static friction force-resulted centripetal acceleration to avoid vehicle saturation effect. This is to calculate vehicle's reference speed at each time step that can ensure safely passing through curvature and adhesion-informed road surfaces. Note that the curvature at a point on the global path can be determined by first fitting a quadratic polynomial to the point and its neighbouring points, and then the curvature is a function of the polynomial's first and second order derivatives. The road adhesive coefficient is determined by, and can be estimated from, two factors—road surface texture and dryness/wetness [20]. The curvature and adhesive coefficient determination process is elaborated in subsection C below. After determining the boundary conditions (vehicle's localisation in the Frenet space and its current reference speed), the vehicle's local trajectories can be sampled by fitting a quintic polynomial to the boundary conditions. Specifically, the local trajectories are sampled under three assumptions about the vehicle's current status, including lane keeping, lane changing and lead vehicle following. After sampling, the local trajectories are provided to the trajectory evaluation level.

For trajectory evaluation, the proposed approach assesses the sampled trajectories from two aspects—collision check and cost estimation. Collision check is to detect the vehicle's potential collisions with other obstacles (i.e., static obstacles and other traffic participants) along the sampled trajectories. Trajectories implying collisions are rejected from the candidate list and the costs of the collision-free ones are further evaluated. The cost estimation consists of two criteria—vehicle's current distance from lane centre and current-reference speed difference. The collision-free trajectory with minimal cost is determined as the vehicle's execution trajectory. Note that this study concentrates on the method of collision detection, where how to obtain the obstacles' positions and orientation is not a focus of the research. Such information is assumed to be obtained from the vehicle's on-board perception sensors.

B. Vehicle Localisation

Vehicle localisation is a crucial stage of the proposed approach which deals with the waypoints representation of road network and describes a vehicle's position in the Frenet coordinate system. It mainly includes creating global reference path and localising vehicle in the Frenet space.

1) Creating Global Reference Path: This step performs a smooth interpolation of the waypoints representation of road network to form a continuous global reference path. There are two different ways of interpolation: one is parametric interpolant and the other is geometric interpolant [21]. Parametric interpolant is to solve the undetermined coefficients in a particular polynomial function to fit a sequence of known data points (e.g., Lagrange, Hermite methods) [22]. The process forms a closed-form expression for the polynomial as fitted to the data points. Instead, the geometric interpolation method assumes no such hidden closed-form expression to solve for the data points, which inserts a new point between every two points and dynamically adjusts the positions of the newly inserted points to ensure geometric fidelity with reference to the desired shape [23]. This offers flexibility than the parametric method to represent the desired shape that the data points imply [24]. Given that a road segment could contain irregular shapes and free-forms which might not all imply suitable closed-form solutions, the geometric interpolation method was used in this research.

After receiving the waypoints data, the approach is built to ensure the second-order of the interpolated global path's geometric continuity (i.e., G2-continuity). G2-continuity implies that the rate of curvature change at each point along the interpolated path is equal, which is a necessary condition to prevent jerks in the path [25]. The G2-continuity is enabled by interpolating midpoints between consecutive waypoints. The positioning of the midpoints is determined with two constraints as shown in Fig. 2: 1) the midpoint P_{AB} is placed on the perpendicular bisector between the consecutive waypoints A and B; 2) the included angle δ_{P} of the midpoint P_{AB} is the arithmetic mean of the waypoints A and B's included angles δ_{A} and δ_{B}.

According to the above constraints, the positioning coordinate $(P_{\mathrm{ABx}}, P_{\mathrm{ABy}})$ of the interpolant P_{AB} can be computed as follows:

$$\begin{cases} P_{\mathrm{ABx}} = \tan\gamma \left| A_{\mathrm{y}} - C_{\mathrm{y}} \right| \\ P_{\mathrm{ABy}} = C_{\mathrm{y}} \end{cases} \tag{1}$$

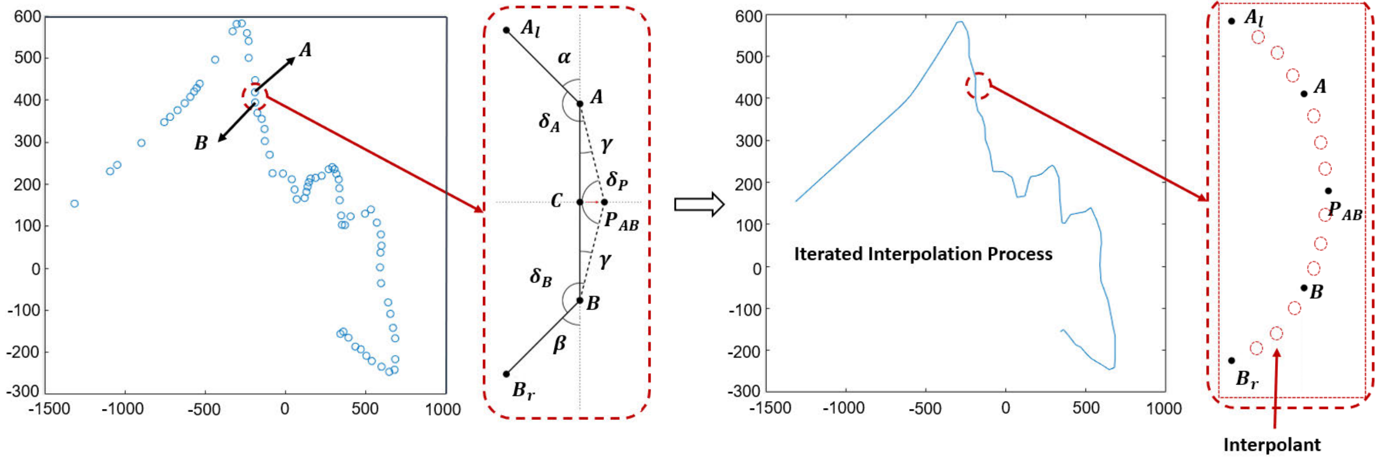

Fig. 2. Iterated interpolation process.

$$\text{where: } \begin{cases} \alpha = \arctan\left(\dfrac{|A_{\mathrm{x}} - A_{\mathrm{lx}}|}{|A_{\mathrm{y}} - A_{\mathrm{ly}}|}\right) \\ \beta = \arctan\left(\dfrac{|B_{\mathrm{x}} - B_{\mathrm{rx}}|}{|B_{\mathrm{y}} - B_{\mathrm{ry}}|}\right) \\ \delta_{\mathrm{A}} = \pi - \alpha + \gamma \\ \delta_{\mathrm{B}} = \pi - \beta + \gamma \\ \delta_{\mathrm{P}} = \dfrac{\delta_{\mathrm{A}} + \delta_{\mathrm{B}}}{2} \\ \gamma = \dfrac{\pi - \delta_{\mathrm{P}}}{2} \\ C_{\mathrm{y}} = \dfrac{A_{\mathrm{y}} + B_{\mathrm{y}}}{2} \end{cases} \tag{2}$$

where $(A_{\mathrm{x}}, A_{\mathrm{y}})$, $(B_{\mathrm{x}}, B_{\mathrm{y}})$, $(C_{\mathrm{x}}, C_{\mathrm{y}})$ and $(P_{\mathrm{ABx}}, P_{\mathrm{ABy}})$ are the coordinates of points A, B, midpoint of AB and the interpolant P_{AB} in the Cartesian space; $(A_{\mathrm{lx}}, A_{\mathrm{ly}})$ and $(B_{\mathrm{rx}}, B_{\mathrm{ry}})$ are the coordinates of points A and B's left and right neighbours A_{l} and B_{r} in the set S_{i}; α is the angle between $A_{\mathrm{l}}A$ and AB, β is the angle between BB_{r} and AB; δ_{A}, δ_{B} and δ_{P} are the included angles of points A, B and P_{AB}; γ is the angle between AP_{AB} and AB.

The interpolation process is iterated and terminates when a predefined criterion is reached: the differences of waypoints' included angles between two successive iterations is less than the threshold—0.01 degree. This threshold is to ensure that the increments of waypoints' included angles are no longer obvious and the interpolated path approaches smooth.

2) Localising Vehicle in the Frenet Space: This step concerns with converting the vehicle's position $P(x, y)$ as obtained in the Cartesian space to the Frenet coordinate $P(s, d)$. This is enabled by first retrieving the point on the global reference path that is closest to the ego vehicle's position in the Cartesian space. The closest point is then marked as the anchor point for the coordinate conversion. To improve the computational efficiency for retrieving the closest point, the proposed approach takes a two-step scheme as illustrated in Fig. 3. First, the vehicle's position is compared with the vertexes of the axis-aligned bounding boxes (AABBs) of each segment along the global path as separated by the waypoints. The AABB method is to generate bounding box to represent the min and max values of the projection of an object on the x, y, and z axes, and functions in an axis-aligned manner (i.e., not rotated with respect to the axes) [26]. The comparison identifies the path segment that is closest to the vehicle's location. Second, the vehicle's position is compared with the interpolated points in the segment to identify the closest point on the segment as the Cartesian-Frenet conversion anchor point.

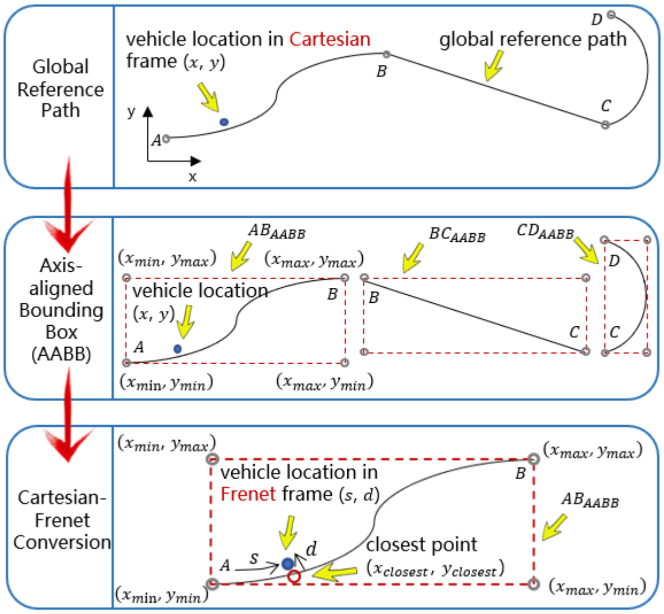

Fig. 3. Cartesian-Frenet conversion.

After identifying the closest point $P(x_{\mathrm{clst}}, y_{\mathrm{clst}})$, the vehicle's position $P(x, y)$ in the Cartesian space is converted to the Frenet coordinate $P(s, d)$ as follows:

$$\begin{cases} s = \displaystyle\sum_{i=2}^{clst} \sqrt{(x_{\mathrm{i}} - x_{\mathrm{i\text{-}1}})^2 + (y_{\mathrm{i}} - y_{\mathrm{i\text{-}1}})^2} \\ d = \sqrt{(x - x_{\mathrm{clst}})^2 + (y - y_{\mathrm{clst}})^2} \end{cases} \tag{3}$$

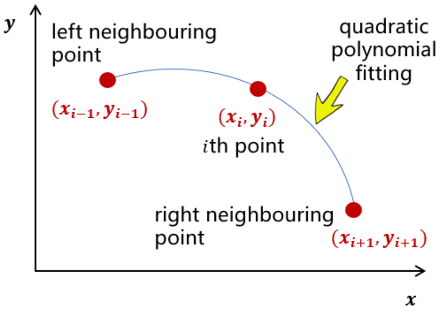

Fig. 4. Quadratic polynomial fitting.

where the s value of the Frenet coordinate $P(s, d)$ is the vehicle's run length along the global path, which is calculated as the cumulative Euclidean distance between the consecutive points (i.e., $(x_{\text{i-1}}, y_{\text{i-1}})$, $(x_{\text{i}}, y_{\text{i}})$) on the global path until the closest point $P(x_{\text{clst}}, y_{\text{clst}})$ is reached; the d value of the Frenet coordinate $P(s, d)$ is the vehicle's offset distance from the global path d, which is calculated as the Euclidean distance between the vehicle's position $P(x, y)$ and the closest point $P(x_{\text{clst}}, y_{\text{clst}})$.

C. Trajectory Generation

Trajectory generation deals with the time-varying road curvature and adhesive coefficients for safe speed estimation and samples the vehicle's local trajectories. It mainly includes calculating vehicle reference speed and sampling local trajectories.

1) Calculating Vehicle Reference Speed: This step mathematically formulates the relationship between vehicle speed and time-varying road curvature and adhesive coefficients. The curvature at a point on the global path is determined in the Cartesian space. It is calculated by first fitting a quadratic polynomial to the point as well as its neighbouring points as shown in Fig. 4, and then the curvature is a function of the polynomial's first and second order derivatives as follows:

$$\rho = \frac{x''y' - x'y''}{((x')^2 + (y')^2)^{(3/2)}} \tag{4}$$

$$\text{where:} \begin{cases} x = a_1 + a_2 t + a_3 t^2 \\ y = b_1 + b_2 t + b_3 t^2 \\ x' = \left.\dfrac{dx}{dt}\right|_{\text{t=0}} = a_2 \\ x'' = \left.\dfrac{d^2x}{dt^2}\right|_{\text{t=0}} = 2a_3 \\ y' = \left.\dfrac{dy}{dt}\right|_{\text{t=0}} = b_2 \\ y'' = \left.\dfrac{d^2y}{dt^2}\right|_{\text{t=0}} = 2b_3 \end{cases} \tag{5}$$

where ρ is curvature coefficient; a_1, a_2, a_3, b_1, b_2 and b_3 are the parameters of the quadratic polynomials; t is the travel time between the consecutive points.

TABLE I

Reference Table for Road Adhesive Coefficient, Road Surface Texture, and Dryness/Wetness Conditions

Texture	Dry/Wet	Adhesive Coefficient
Abrased Asphalt	Dry	0.43
	Wet	0.40
Smooth Asphalt	Dry	0.55
	Wet	0.40
New Asphalt	Dry	0.65
	Wet	0.45
Abrased Concrete	Dry	0.50
	Wet	0.35
Smooth Concrete	Dry	0.60
	Wet	0.45
New Concrete	Dry	0.70
	Wet	0.50
Grass	Dry	0.35
	Wet	0.17
Loose Snow	Dry	0.10
	Wet	0.30
Compact Snow	Dry	0.25
	Wet	0.30
Ice	Dry	0.05
	Wet	0.08

The road adhesive coefficient is determined by two factors—road surface texture and dryness/wetness. Note that this study focuses on the establishment of vehicle speed's relationship with road curvature and adhesive coefficients, where how to obtain the road surface texture and dryness/wetness conditions is not a focus of the research. Such information is assumed to be obtained from the vehicle's on-board perception sensors. After obtaining the road surface texture and dryness/wetness conditions, the value of road adhesive coefficient is determined by the reference table suggested by Leng et al. [27], as provided in Table I.

After determining the current road curvature and adhesive coefficients, the relationship between vehicle speed, road curvature and adhesive coefficients can be established. According to the physics of circular motion [28], the centripetal force is a net force that acts on a body to keep it moving along a circular path. The velocity of the moving body experiences a centripetal acceleration $a_c(t)$ directed toward the center of its path. The acceleration $a_c(t)$ changes in both magnitude and direction with respect to the moving body's longitudinal reference speed $v_s(t)$ and looking direction (i.e., curvature $\rho(t)$), respectively, as shown in formula (6). The centripetal acceleration $a_c(t)$ is provided by the maximal static friction $F_c^{max}(t)$ with a reduction rate k to avoid vehicle saturation effect, as shown in formula (7).

$$a_{\text{c}}(t) = v_s(t)^2 \rho(t) \tag{6}$$

$$\text{where:} \begin{cases} a_c(t) = k a_c^{max}(t) \\ a_c^{max}(t) = \dfrac{F_c^{max}(t)}{m} \\ F_c^{max}(t) = \eta(t) m g \end{cases} \tag{7}$$

where $a_c(t)$ is centripetal acceleration at time t; $v_s(t)$ is the calculated vehicle reference speed at time t along the longitudinal direction s in Frenet space; $\rho(t)$ is road curvature at time t; $F_c^{max}(t)$ is the maximal centripetal force as provided by the maximal static friction at time t; $\eta(t)$ is road adhesive coefficient at time t; m is the vehicle's mass; g is gravitational acceleration; $a_c^{max}(t)$ is the maximal centripetal acceleration as provided by the maximal static friction at time t; k is the reduction rate to the maximal centripetal acceleration to avoid vehicle saturation effect.

Thus, the centripetal acceleration $a_c(t)$ specifies the computational relationship between the vehicle reference speed, road curvature and adhesion. From formulas (6)-(7), it can be inferred that $v_s(t) = \sqrt{k\eta(t)g/\rho(t)}$, and k is the reduction rate to the maximal centripetal acceleration to avoid vehicle saturation effect. As Ali et al. [29] pointed out, when the coefficient $k \leq 0.4$, the response of vehicle states to the driver input is approximately linear and the vehicle is usually stable. Otherwise, the vehicle's tyres approach their saturation threshold and do not react to driving commands linearly. Based on the findings, this research uses the coefficient $k = 0.4$ as the threshold to formulate the relationship between vehicle speed, road curvature and adhesive coefficients. The relationship is as follows:

$$v_s(t) = \begin{cases} v_0 & v_0^2\rho(t) \leq 0.4\eta(t)g \\ \sqrt{\dfrac{0.4\eta(t)g}{\rho(t)}} & v_0^2\rho(t) > 0.4\eta(t)g \end{cases} \tag{8}$$

where v_0 is the vehicle's initial or predefined speed; $\rho(t)$ is the road curvature when the vehicle travels along the road at time t in Frenet space; $v_s(t)$ is the calculated vehicle reference speed at time t along the longitudinal direction s in Frenet space—vehicle's reference speed to ensure safety at the current location with known road curvature and adhesive conditions; $\eta(t)$ is road adhesive coefficient at time t; g is gravitational acceleration.

2) Sampling Local Trajectories: In this step, the preview distance for sampling the local trajectory of the vehicle is determined using the reference speed of the vehicle and the preview time. The local trajectory of the vehicle is then sampled using the preview distance and the current position of the vehicle in the Frenet space $P(s, d)$ as boundary conditions. The preview time is a hyper-parameter, where a smaller or larger preview time indicates a myopic or non-myopic trajectory planning mode, respectively. The proposed approach uses the quartic polynomial for trajectory sampling. The boundary conditions for the quartic polynomial are five-fold: the start position, speed and acceleration of the vehicle; and the end position and speed of the vehicle. Specifically, the start position is the current position of the vehicle $P(s, d)$. The end position is the current position of the vehicle $P(s, d)$ with the preview distance added. The start and end speeds of the vehicle can be determined by formula (8) using the determined road curvature and the adhesion coefficients at the start and end positions. The start acceleration is the current acceleration of the vehicle, which can be read from the built-in inertial measurement unit (IMU).

Based on the Frenet coordinate system (s, d), the sampling of the trajectory is decomposed into the longitudinal s and lateral d directions. The quartic polynomial equations for the two directions are as follows:

$$\begin{cases} s(t) = c_0 + c_1t + c_2t^2 + c_3t^3 + c_4t^4 \\ v_s(t) = c_1 + 2c_2t + 3c_3t^2 + 4c_4t^3 \\ a_s(t) = 2c_2 + 6c_3t + 12c_4t^2 \\ d(t) = e_0 + e_1t + e_2t^2 + e_3t^3 + e_4t^4 \\ v_d(t) = e_1 + 2e_2t + 3e_3t^2 + 4e_4t^3 \\ a_d(t) = 2e_2 + 6e_3t + 12e_4t^2 \end{cases} \tag{9}$$

subject to the known $s(t_0)$, $v_s(t_0)$, $a_s(t_0)$, $s(t_1)$, $v_s(t_1)$, $d(t_0)$, $v_d(t_0)$, $a_d(t_0)$, $d(t_1)$, $v_d(t_1)$; where: $s(t)$, $v_s(t)$ and $a_s(t)$ are the vehicle's longitudinal position, velocity and acceleration at time t; $d(t)$, $v_d(t)$ and $a_d(t)$ are the vehicle's lateral position, velocity and acceleration at time t; t_0 is the starting time (t_0=0); t_1 is the end time for trajectory sampling (which is a hyper-parameter as mentioned); c_0, c_1, c_2, c_3 and c_4 are the five coefficients in the longitudinal quartic polynomial to be solved by given the known $s(t_0)$, $v_s(t_0)$, $a_s(t_0)$, $s(t_1)$, $v_s(t_1)$; e_0, e_1, e_2, e_3 and e_4 are the five coefficients in the lateral quartic polynomial to be solved by given the known $d(t_0)$, $v_d(t_0)$, $a_d(t_0)$, $d(t_1)$, $v_d(t_1)$.

Note that three assumptions are made when sampling the trajectories, including lane keeping, lane changing, and lead vehicle following. The assumptions lead to different end vehicle positions for solving the quartic polynomial equations (9), as shown in Fig. 5.

- For lane keeping, it is assumed that there are no other road users in front of the ego vehicle in the current lane, and that the ego vehicle can continue driving in the current lane at the current speed. Under this assumption, the end position of the ego vehicle in the longitudinal direction is $s(t_1) = s(t_0) + v_s(t_0)t_1$, and the end position in the lateral direction is $d(t_1) = d(t_0)$.
- For lane changing, it is assumed that there are other road users or static obstacles in front of the ego vehicle in the current lane, and that the ego vehicle has to change lanes to drive. Under this assumption, the end position of the ego vehicle in the longitudinal direction is $s(t_1) = s(t_0)+v_s(t_0)t_1$, and the end position in the lateral direction is $d(t_1) = d(t_0) \pm v_d(t_0)t_1$.
- For lead vehicle following, it is assumed that there are other road users in front of the ego vehicle in the current lane, and that the ego vehicle cannot change lanes because the adjacent lanes are also occupied. Under this assumption, the ego vehicle must maintain a safe distance s_{sd} from the lead vehicle's position $s_{ld}(t)$ and drive at the same speed as the lead vehicle. In this case, the end position of the ego vehicle in the longitudinal direction is $s(t_1) = s_{ld}(t_1) - s_{sd}$, and the end position in the lateral direction is $d(t_1) = d(t_0)$.

The sampled trajectories are then all checked for collisions, and trajectories that suggest collisions are removed from the candidate list. The collision checking process is explained in more detail in subsection D below.

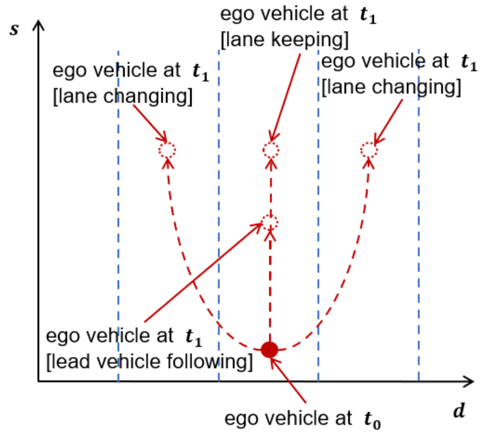

Fig. 5. Trajectory sampling assumptions.

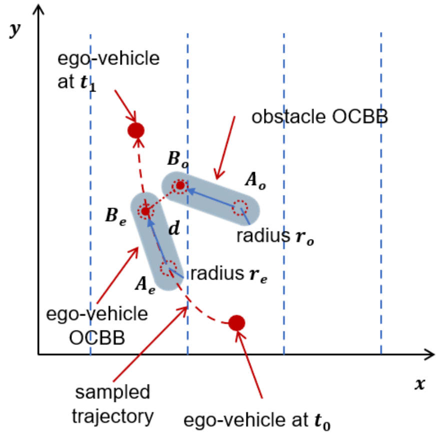

Fig. 7. OCBB-based collision detection.

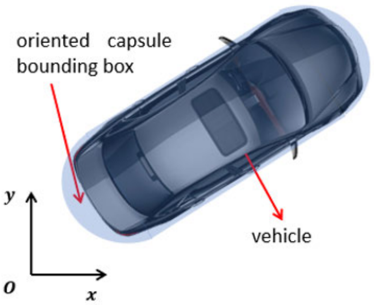

(a) Vehicle wrapping.

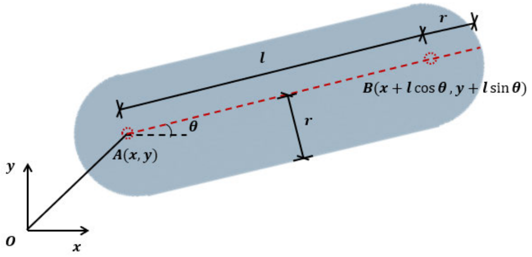

(b) Dimensions.

Fig. 6. Oriented capsule bounding box (OCBB).

D. Trajectory Evaluation

1) Collision Checking for Sampled Trajectories: Given that the shape of capsule suits the geometry of vehicle, this research uses the oriented capsule bounding box (OCBB) to approximate the poses and geometries of the ego vehicle and perceived obstacles for collision checking [30]. OCBB is a type of collision geometry, which is defined by length l, radius r, tangent angle θ, and vertices $A(x, y)$ and $B(x + l\cos\theta, y + l\sin\theta)$, as shown in Fig. 6.

The collision status can then be determined by checking whether the OCBBs of the ego-vehicle and obstacles intersect along the sampled local trajectories. As shown in Fig. 7, the intersection detection is to evaluate whether the shortest distance d between the vectors $\overrightarrow{A_eB_e}$ and $\overrightarrow{A_oB_o}$ that represent the ego vehicle and an obstacle's OCBBs is greater than the sum of the radii r_e and r_o of the OCBBs. If $d \le r_e + r_o$, the OCBBs are intersected and the collision result is thereby positive. The trajectories implying collisions are then rejected from the candidate list. Specifically, the shortest distance d can be determined by respectively calculating the shortest distances between A_e and $\overrightarrow{A_oB_o}$, B_e and $\overrightarrow{A_oB_o}$, A_o and $\overrightarrow{A_eB_e}$, and B_o and $\overrightarrow{A_eB_e}$ and then selecting the minimum value among them as the final shortest distance d. In this research, the calculation of the shortest distance adopts the vector calculus approach. Taking the shortest distance $d_{A_e\overrightarrow{A_oB_o}}$ between the point A_e and the vector $\overrightarrow{A_oB_o}$ as an example, the $d_{A_e\overrightarrow{A_oB_o}}$ can be calculated as follows:

$$k = \frac{\overrightarrow{A_oA_e} \cdot \overrightarrow{A_oB_o}}{|\overrightarrow{A_oB_o}|^2} \tag{10}$$

$$d_{A_e\overrightarrow{A_oB_o}} = \begin{cases} \overrightarrow{A_oA_e} & k \le 0 \\ \overrightarrow{B_oA_e} & k \ge 1 \\ \sqrt{|\overrightarrow{A_oA_e}|^2 - k^2} & 0 < k < 1 \end{cases} \tag{11}$$

where $\overrightarrow{A_oB_o}$, $\overrightarrow{A_oA_e}$ and $\overrightarrow{B_oA_e}$ are the vectors from A_o to B_o, from A_o to A_e, and from B_o to A_e, respectively, as shown in Fig. 7; The formulas (10) and (11) are in the relationship of variable assignment, where the formula (11) is in the form of a piece-wise function and the computed result of formula (10) is assigned to the coefficient k of the conditional statement in formula (11) for function selection. As can be seen in Fig. 7, if $k \le 0$, the projection of A_e on $\overrightarrow{A_oB_o}$ is on the extension line of $\overrightarrow{B_oA_o}$ and the $\overrightarrow{A_oA_e}$ is the shortest distance between A_e and $\overrightarrow{A_oB_o}$. If $k \ge 1$, the projection of A_e on $\overrightarrow{A_oB_o}$ is on the extension line of $\overrightarrow{A_oB_o}$ and the $\overrightarrow{B_oA_e}$ is the shortest distance between A_e and $\overrightarrow{A_oB_o}$. If $0 < k < 1$, the projection of A_e on $\overrightarrow{A_oB_o}$ is within the line segment $\overrightarrow{A_oB_o}$ and the $\sqrt{|\overrightarrow{A_oA_e}|^2 - k^2}$ is shortest distance between A_e and $\overrightarrow{A_oB_o}$.

2) Cost Estimating for Sampled Trajectories: This step establishes a cost function J to further estimate the cost of the sampled trajectories that imply no collisions. The collision-free trajectory with minimal cost is determined as the vehicle's execution trajectory. Specifically, the cost estimation consists of two criteria—vehicle's current distance from lane centre and current-reference speed difference, which is computed

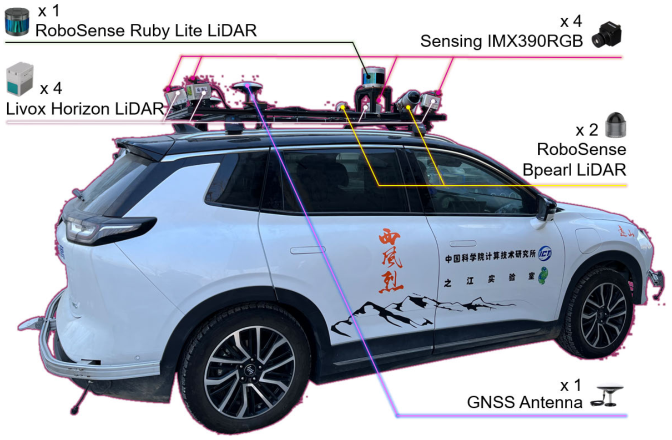

Fig. 8. Test vehicle.

as follows:

$$J = \sum_{t=t_0}^{t_1} (d(t) - d_l(t)) + \sum_{t=t_0}^{t_1} (\hat{v_s}(t) - v_s(t)) \tag{12}$$

where J is the estimated cost; $d(t)$ is the vehicle's lateral position at time t; $d_l(t)$ is the position of the lane centre at time t; $\hat{v_s}$(t) is vehicle's current speed at time t (which can be estimated as the vehicle's travel distance in unit time dt, where the travel distance can be obtained from the vehicle's on-board visual odometry); $v_s(t)$ is the vehicle's observed speed at time t as calculated from known road curvature and adhesive conditions; t_0 is the starting time of the local trajectory ($t_0 = 0$); t_1 is the end time of the local trajectory (which is a hyper-parameter as mentioned).

III. EXPERIMENT AND RESULTS

In the experiment, we aimed to test the proposed method for curvature and adhesion adaptability. As shown in Fig. 8, our test vehicle was equipped with four Livox Horizon LIDARs, two RoboSense Bpearl LiDARs, one RoboSense Ruby Lite LiDAR, four Sensing IMX390RGB cameras, and one GNSS Antenna. However, given the hazardous nature of challenging road conditions, the on-board testing was unsafe and contained the potential risk of physical harm. Thus, the experiment was performed in a simulated mountainous driving environment using Unreal Engine 4.25 and Simulink, as shown in Fig. 9. Algorithms of the proposed approach was implemented in Matlab scripts running on a PC with an AMD Ryzen 7 4800H processor at 2.9 GHz and 16 GB RAM. In the simulated environment, two representative driving scenarios were implemented, namely sharp turn and ice-covered road surface. The two scenarios were used to test the proposed method for curvature and adhesion adaptability, respectively. The road and test vehicle in the environment were sufficiently simulated to achieve a closing of the sim-2-real gap as much as possible. That is, the simulated road property did not incorporate simplified assumptions such as frictionless surfaces. In addition, the physical parameters of the simulation vehicle were calibrated to represent the test vehicle in reality, including the mass, centre of mass, inertia, stiffness, damping, longitudinal distances from centre of mass to front and rear axles, longitudinal velocity tolerance, and aerodynamic coefficients. Besides, the vehicle dynamics were also analysed using CarSim, which mathematically computes the driver controls of simulation vehicles in a way that mimics how a vehicle would respond to traffic situations as in the real world.

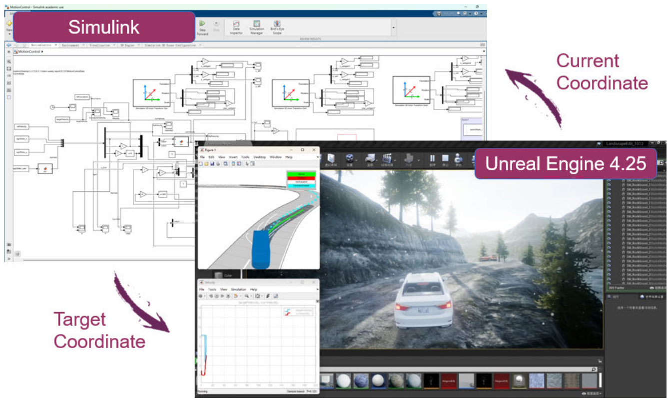

Fig. 9. Simulated driving environment using Unreal Engine 4.25 and Simulink.

The experiment also made a comparison with the state-of-the-art approaches in the existing studies. Since our method is in relation to time-varying road curvature and adhesion (TRCA) conditions, it is abbreviated and mentioned as TRCA in the comparison. As introduced in section I, the determination of the vehicle speed in the existing methods can be described on three levels: 1) dynamic adaptation—with respect to predefined value/boundary, 2) dynamic adaptation—with respect to road curvature, and 3) dynamic adaptation—with respect to road adhesion. In the experiment, we compared our method with the prior approaches in each level that use representative techniques and indicate good numbers of citation counts. The compared approaches consisted of MPC by Liu et al. [10], RDNN + DRL by Chai et al. [14], Hybrid A* by Li et al. [18], and TRCA (our approach), as listed in Table II. The more detailed interpretation of the prior methods can be found in section I.

After testing the curvature and adhesion adaptability, the model uncertainty of our proposed method was evaluated at last. The testing results are discussed in detail below.

A. Curvature Adaptability

The curvature adaptability of our approach was tested in a sharp turn driving scenario, as presented in Fig. 10a. The road texture was abrased and dry asphalt. According to Table I, the adhesion coefficient was 0.43. The centreline of the road was chosen as the global reference path, which was approximately 112 meters long. The road consisted of two lanes in opposite directions, and the lane width was 3.35 meters. The direction of travel in the experiment was from point $A(149.52,342.11)$ to $B(123.35,404.31)$, as illustrated in Fig. 10b. The largest curvature on the path was 0.2388, which formed a sharp turn. Since in many countries (e.g., Switzerland [31], Sweden [32], China [33]) 30 km/h (≈ 8.33 m/s) is prescribed as the speed limit for road turns, the initial reference speed of the vehicle in the sharp turn test was set to 8.33 m/s.

TABLE II

BRIEF INFORMATION OF THE COMPARED STUDIES

Levels	Features	Studies	Methods
Level I	Speed dynamic adaptation—with respect to predefined value/boundary.	Liu et al. [10]	MPC
Level II	Speed dynamic adaptation—with respect to road curvature.	Chai et al. [14]	RDNN + DRL
Level III	Speed dynamic adaptation—with respect to road adhesion.	Li et al. [18]	Hybrid A*
Level IV	Speed dynamic adaptation—with respect to road curvature and adhesion.	Our approach.	TRCA (our approach)

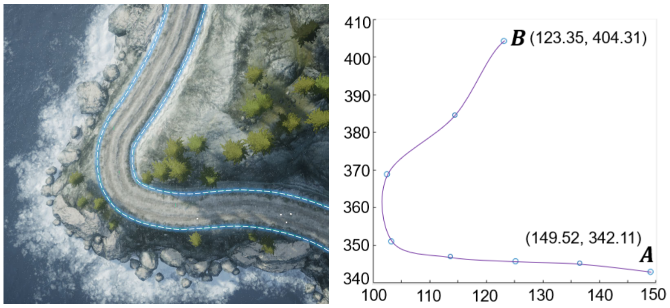

(a) Top view. (b) Global reference path.

Fig. 10. Sharp turn driving scenario.

The four approaches in Table II were implemented in the sharp turn driving scenario. The following aspects were used to compare the performance of the four approaches: safety and comfort, structural similarity, and planning efficiency. Specifically, the quantitative measures of safety and comfort consisted of maximum deviation, average deviation, completeness level, and speed statistics. The quantitative measures of structural similarity consisted of Fréchet distance and Equidirectional, which basically indicate the general fitness of a planned trajectory for a given reference path. The quantitative measure of planning efficiency consisted of frequency statistics. The annotations of the quantitative measures are as follows.

- Maximum deviation is an absolute value which measures the maximum lateral deviation of a planned trajectory from the road centre along the global path [34].
- Average deviation is also a metric in the form of absolute value which calculates the average lateral deviation of a planned trajectory from the road centre along the global path [35].
- Completeness level indicates the proportion of distance successfully traveled by the vehicle in the global path before exceeding lane boundaries [36].
- Speed statistics describe the statistical features of the reference speed of the vehicle along the planned trajectory, namely, mean and variance [37].
- Fréchet distance is a measure of closeness between two curves (e.g., a planned trajectory X_P and the global path X_G) in terms of the spacing between their inflection points [38]. It is defined as the minimum cord-length sufficient to join a point traveling forward along X_P and one traveling forward along X_G, although the rate of travel for either point may not necessarily be uniform.
- Equidirectional uses Pearson correlation coefficient to measure the co-movement direction of a planned trajectory in relation to the concave-convex fluctuations of the global path [39]. If the correlation is positive, the growing trend of the planned trajectory is considered equidirectional to the global path, and a stronger correlation indicates a greater equivalence of the underlying trend. Otherwise, the opposite.
- Frequency statistics describe the statistical features of the re-planning frequencies during a model run session, namely, mean and variance Chai et al. [14].

The planned trajectories by the four approaches are shown in Fig. 11a-11d. The results of the quantitative measures of the planned trajectories are provided in Table III, which are interpreted in detail below.

1) Safety and Comfort: The test results of safety and comfort are provided in Rows 2-5 in Table III. First, the Hybrid A* approach indicated the minimal degree of deviations (maximum: 1.3211 metres, average: 0.9135 metres), followed by TRCA (our method) (maximum: 2.2516 metres, average: 1.6432 metres), then RDNN + DRL (maximum: 2.3342 metres, average: 1.7276 metres) and MPC (maximum: 2.5134 metres, average: 1.9254 metres). Second, TRCA (our method) outperformed the other approaches in terms of completeness, in which the vehicle remained in the lane at all times and successfully completed the whole length of the global path from A to B. Whereas, the MPC, RDNN + DRL and Hybrid A* approaches resulted in the vehicle exceeding the lane boundaries at locations of (107.25,383.14), (104.13,379.21) and (109.25,384.55) with level of completeness of 77.72%, 75.31% and 79.53%, respectively. To illustrate, the locations of completeness by each approach are marked by the divergence points C in Fig. 11a-11d. From the results of the first three metrics, it can be inferred that our approach was able to generate a safe and comfort trajectory in the sharp turn scenario, in which the vehicle was guided to successfully pass through the global path without producing large deviations and exceeding lane boundaries.

The reference speed generated by the four approaches was also compared at each time step. The results showed that TRCA (our method) was able to greatly reduce the vehicle's reference speed to ensure safe passing of road sections with large curvature values, as presented in Fig. 12. The other approaches were unable to regulate the vehicle's reference speed towards a modest extent at the location of the most severe curvature, resulting in the vehicle speeding out of the lane at the divergence location C, as shown in Fig. 11a-11c. Besides, the speed statistics (Row 5 in Table III) show that the reference speed along the planned trajectory by TRCA (our method) was on average smaller and more spread out ($\mu = 5.1324$, $\sigma^2 = 4.9861$). This manifests that our approach prioritises safety at a sacrifice of manoeuvre efficiency.

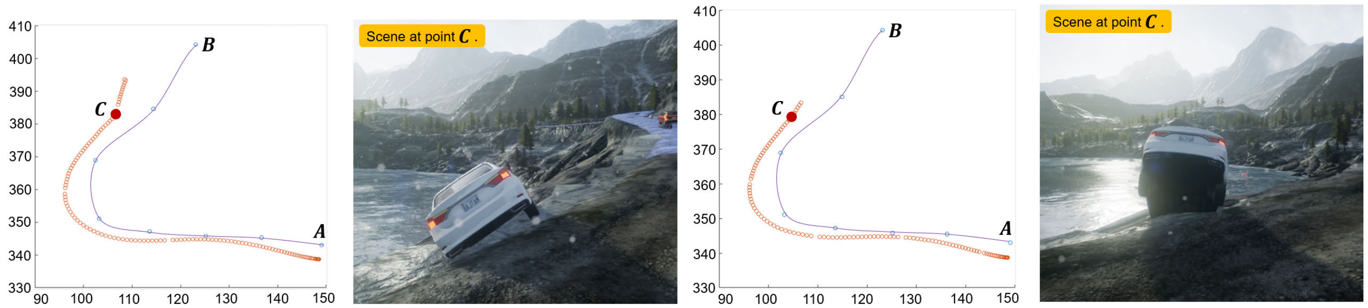

(a) MPC (b) RDNN + DRL

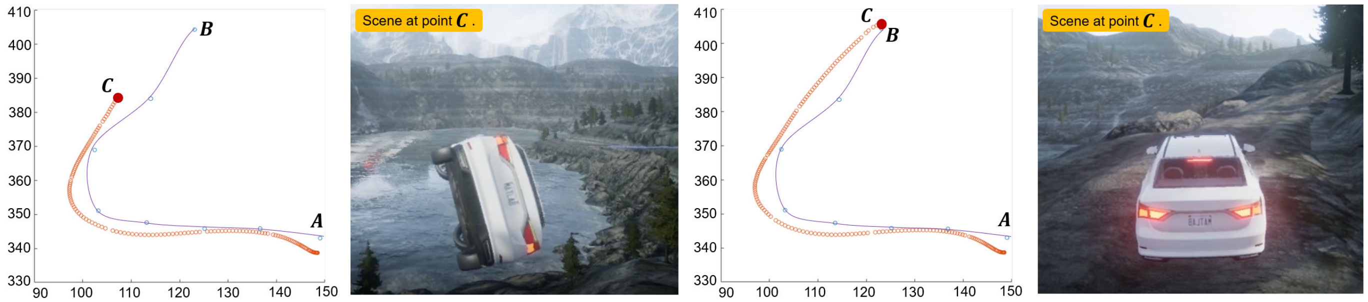

(c) Hybrid A* (d) TRCA (our approach)

Fig. 11. Vehicle executed trajectories for the sharp turn driving scenario (at 8.33 m/s initial speed): a) MPC approach; b) RDNN + DRL approach; c) Hybrid A* approach; d) TRCA approach (our approach).

TABLE III

Curvature Adaptability Test Results

Measures	Sub-measures	MPC	RDNN + DRL	Hybrid A*	TRCA (our approach)
Safety and Comfort	Maximum Deviation	2.5134	2.3342	**1.3211**	2.2516
	Average Deviation	1.9254	1.7276	**0.9135**	1.6432
	Completeness Level	77.72% C(107.25,383.14)[a]	75.31% C(104.13,379.21)[a]	79.53% C(109.25,384.55)[a]	**100.00% C(123.66,404.72)[a]**
	Speed Statistics	μ = 8.3300, σ^2 = 0.0000	μ = 7.6213, σ^2 = 1.1234	μ = 7.1152, σ^2 = 1.3152	**μ = 5.1324, σ^2 = 4.9861**
Structural Similarity	Fréchet Distance	3.6569	2.4355	1.6033	**1.5938**
	Equidirectional	0.8354	0.8632	**0.9424**	0.9371
Planning Efficiency	Frequency Statistics	μ = 12.0365, σ^2 = 3.6517	μ = 9.2552, σ^2 = 3.1528	μ = 11.1529, σ^2 = 4.1328	**μ = 14.0264, σ^2 = 2.1766**

Note: [a] Locations of completeness are marked by points C in Fig. 11a-11d.

2) Structural Similarity: The test results of structural similarity are provided in Rows 6-7 in Table III. As can be seen, TRCA (our method) indicated the minimum Fréchet distance of 1.5938. This implied a higher degree of closeness between the planned trajectory by TRCA (our method) and the global reference path in terms of the spacing between their inflection points, than the other approaches. In addition, we used the Pearson correlation coefficient to compare the level of equidirectional of the planned trajectories' co-movement directions by the four approaches in relation to the concave-convex fluctuations of the global reference path. The result of TRCA (our method) (0.9371) was almost identical to the Hybrid A* approach (0.9424), and was higher than RDNN + DRL (0.8632) and MPC (0.8354). This implied that the growing trend of the planned trajectory by TRCA (our method) was considerably equidirectional to the global path.

3) Planning Efficiency: The test results of planning efficiency are provided in Row 8 in Table III. The frequency statistics show that the re-planning frequencies of TRCA (our method) was on average higher and less spread out ($\mu = 14.0264$, $\sigma^2 = 2.1766$), followed by MPC ($\mu = 12.0365$, $\sigma^2 = 3.6517$), then Hybrid A* ($\mu = 11.1529$, $\sigma^2 = 4.1328$) and RDNN + DRL ($\mu = 9.2552$, $\sigma^2 = 3.1528$). This manifests an efficient and steady re-planning rate of our approach.

B. Adhesion Adaptability

The adhesion adaptability of our approach was tested in a driving scenario with ice-covered road surfaces, as presented in Fig. 13a. The road texture was iced-covered and dry. According to Table I, the adhesion coefficient was 0.05. The centreline of the road was chosen as the global reference path, which was approximately 101 meters long. The road consisted of two lanes in opposite directions, and the lane width was 3.35 meters. The direction of travel in the experiment was from point A(129.53,494.12) to B(107.12,568.34), as illustrated in Fig. 13b. The largest curvature on the path was 0.0539. Since it has been advised to avoid speeding over 30 km/h ($\approx$ 8.33 m/s) on icy roads [40], the initial reference speed of the vehicle in the ice-covered testing scenario was set to 8.33 m/s.

The four approaches in Table II were implemented in the ice-covered driving scenario. The planned trajectories by the four approaches are provided in Fig. 14a-14d. Table IV

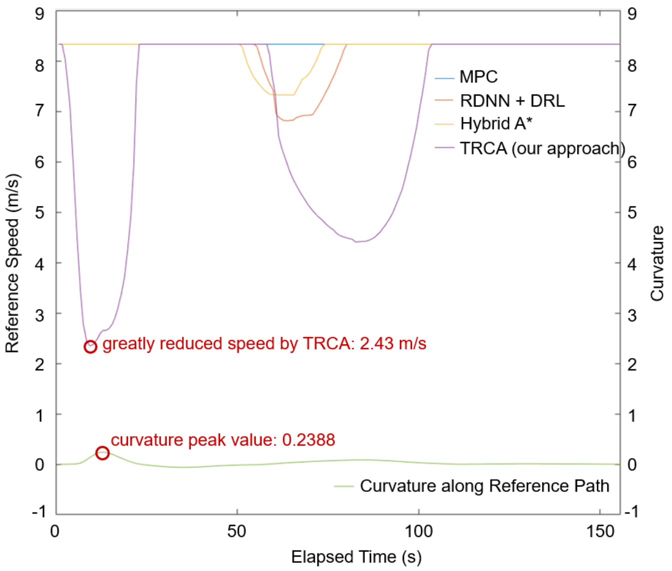

Fig. 12. Reference speed at each elapsed time step by MPC, RDNN + DRL, Hybrid A* and TRCA (our method) in comparison with curvature along reference path.

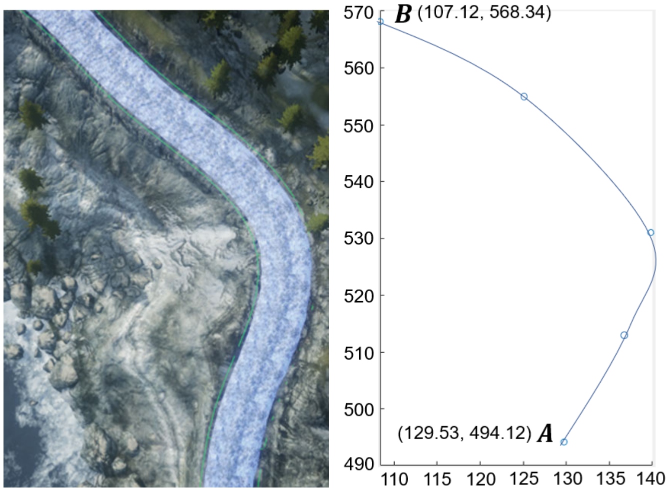

(a) Top view. (b) Global reference path.

Fig. 13. Ice-covered driving scenario.

presents the results of the quantitative measures of the planned trajectories, including safety and comfort, structural similarity, and planning efficiency. The results are interpreted in detail below.

1) Safety and Comfort: The test results of safety and comfort are provided in Rows 2-5 in Table IV. First, the Hybrid A* approach indicated the minimal degree of deviations (maximum: 1.3412 metres, average: 0.9214 metres), followed by TRCA (our method) (maximum: 1.4235 metres, average: 0.9345 metres), then MPC (maximum: 3.1523 metres, average: 2.2135 metres) and RDNN + DRL (maximum: 3.2156 metres, average: 2.1345 metres). Second, TRCA (our method) and Hybrid A* outperformed the other approaches in terms of completeness, in which the vehicle remained in the lane at all times and successfully completed the whole length of the global path from A to B. Whereas, the MPC and RDNN + DRL approaches resulted in the vehicle exceeding the lane boundaries at locations of (137.98,553.11) and (138.12,552.65) with level of completeness of 46.23% and 45.12%, respectively. To illustrate, the locations of completeness by each approach are marked by the divergence points C in Fig. 14a-14d. From the results of the first three metrics, it can be inferred that our approach was able to generate a safe and comfort trajectory in the ice-covered driving scenario, in which the vehicle was guided to successfully pass through the global path without producing large deviations and exceeding lane boundaries.

The reference speed generated by the four approaches was also compared at each time step. The results showed that TRCA (our method) and Hybrid A* were able to greatly reduce the vehicle's reference speed to ensure safe passing of road sections with poor adhesion conditions, as presented in Fig. 15. The other approaches were unable to regulate the vehicle's reference speed towards a modest extent, resulting in the vehicle speeding out of the lane at the divergence location C, as shown in Fig. 14a-14b. Besides, the speed statistics (Row 5 in Table IV) show that the reference speed along the planned trajectory by TRCA (our method) was on average smaller and more spread out ($\mu = 4.7136$, $\sigma^2 = 5.2526$). This manifests that our approach prioritises safety at a sacrifice of manoeuvre efficiency.

2) Structural Similarity: The test results of structural similarity are provided in Rows 6-7 in Table IV. As can be seen, TRCA (our method) indicated the minimum Fréchet distance of 1.6234. This implied a higher degree of closeness between the planned trajectory by TRCA (our method) and the global reference path in terms of the spacing between their inflection points, than the other approaches. In addition, we used the Pearson correlation coefficient to compare the level of equidirectional of the planned trajectories' co-movement directions by the four approaches in relation to the concave-convex fluctuations of the global reference path. The result of TRCA (our method) (0.9376) was almost identical to the Hybrid A* approach (0.9253), and was higher than MPC (0.8934) and RDNN + DRL (0.8825). This implied that the growing trend of the planned trajectory by TRCA (our method) was considerably equidirectional to the global path.

3) Planning Efficiency: The test results of planning efficiency are provided in Row 8 in Table IV. The frequency statistics show that the re-planning frequencies of TRCA (our method) was on average higher and less spread out ($\mu = 13.8453$, $\sigma^2 = 2.7833$), followed by MPC ($\mu = 12.3531$, $\sigma^2 = 3.2315$), then Hybrid A* ($\mu = 11.3568$, $\sigma^2 = 4.2513$) and RDNN + DRL ($\mu = 9.7952$, $\sigma^2 = 3.7953$). This manifests an efficient and steady re-planning rate of our approach.

C. Model Uncertainty

Uncertainty refers to the variability and sureness of an event (e.g., the performance of a model on a given dataset). As Radev et al. [41] noted, decision models that are either learning or mechanistic derive different sources of uncertainty. A learning model (e.g., deep neural networks) tunes its parameters to approximate an unknown function from a set of input-output data pairs, which are subject to epistemic

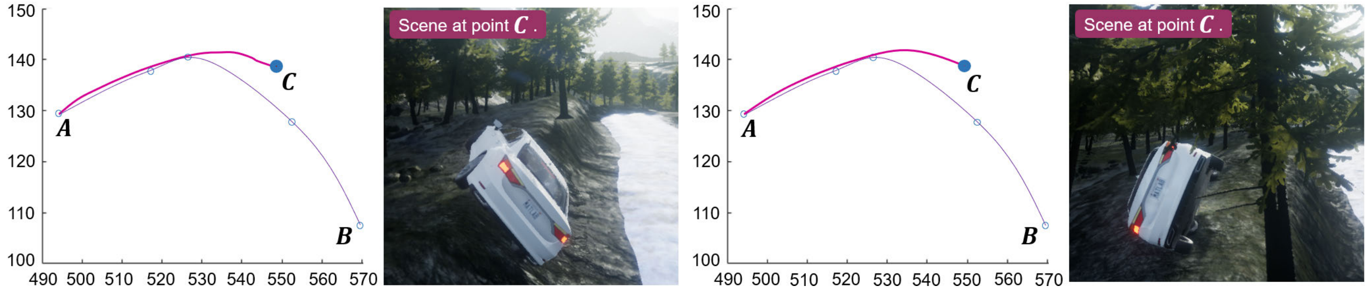

(a) MPC (b) RDNN + DRL

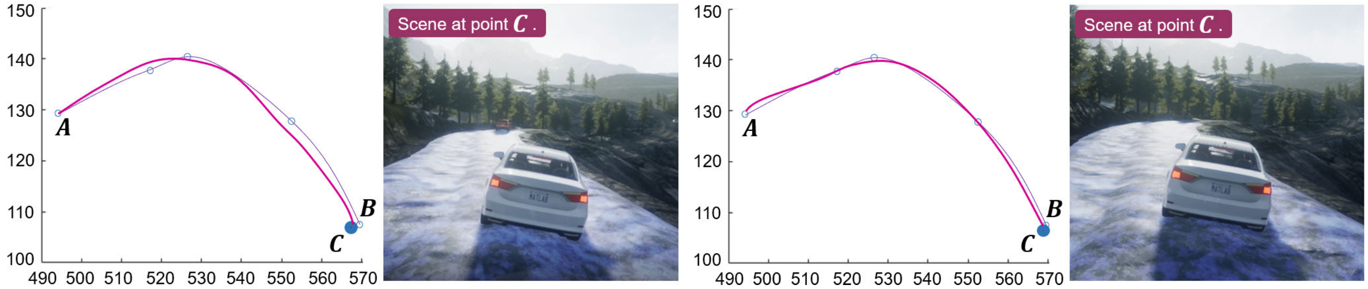

(c) Hybrid A* (d) TRCA (our approach)

Fig. 14. Vehicle executed trajectories for the ice-covered driving scenario (at 8.33 m/s initial speed): a) MPC approach; b) RDNN + DRL approach; c) Hybrid A* approach; d) TRCA approach (our approach).

TABLE IV

ADHESION ADAPTABILITY TEST RESULTS

Measures	Sub-measures	MPC	RDNN + DRL	Hybrid A*	TRCA (our approach)
Safety and Comfort	Maximum Deviation	3.1523	3.2156	**1.3412**	1.4235
	Average Deviation	2.2135	2.1345	**0.9214**	0.9345
	Completeness Level	46.23% $C(137.98,553.11)^{a}$	45.12% $C(138.12,552.65)^{a}$	100.00% $C(107.98,567.37)^{a}$	**100.00%** $\boldsymbol{C(106.78,569.11)^{a}}$
	Speed Statistics	$\mu = 8.3300$, $\sigma^2 = 0.0000$	$\mu = 8.3300$, $\sigma^2 = 0.0000$	$\mu = 6.7832$, $\sigma^2 = 3.6738$	$\boldsymbol{\mu = 4.7136}$, $\boldsymbol{\sigma^2 = 5.2526}$
Structural Similarity	Fréchet Distance	3.8215	3.9812	1.7452	**1.6234**
	Equidirectional	0.8934	0.8825	**0.9253**	0.9376
Planning Efficiency	Frequency Statistics	$\mu = 12.3531$, $\sigma^2 = 3.2315$	$\mu = 9.7952$, $\sigma^2 = 3.7953$	$\mu = 11.3568$, $\sigma^2 = 4.2513$	$\boldsymbol{\mu = 13.8453}$, $\boldsymbol{\sigma^2 = 2.7833}$

Note: ^{a} Locations of completeness are marked by points C in Fig. 14a-14d.

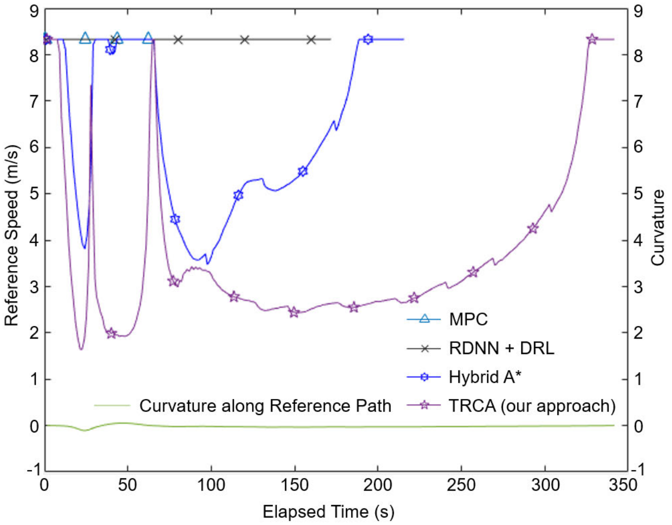

Fig. 15. Reference speed at each elapsed time step by MPC, RDNN + DRL, Hybrid A* and TRCA (our method) in comparison with curvature along reference path.

and aleatory uncertainties [42], [43]. Epistemic uncertainty refers to the imperfect knowledge of a learning model and is often caused by the lack of training data for a particular phenomenon [44]. Aleatory uncertainty accounts for the inherent randomness of a training process, such as randomness in the selection of mini-batches of data or in the application of gradients, dropouts and noise injections [45]. For example, stochastic gradient descent (SGD) introduces randomness by shuffling the training data and randomly selecting batches, and dropout randomly disables a subset of neurons during training to prevent overfitting. Mechanistic models, on the other hand, are described by explicitly stated processes and formulas based on established scientific abstractions of physical, chemical and biological principles [46]. Previous studies have shown that uncertainty in mechanistic modelling stems from input sources [47], [48]. Input uncertainty illustrates that there could be uncertainty in the input variables that causes uncertainty in the model outputs [41].

Since formulas (1)-(12) are mathematical expressions for equivalent geometric and physical processes, our approach is mechanistic rather than a learning model. To assess the uncertainty of our model, we followed the approaches described in a frequently cited comparative review in this collection by Uusitalo et al. [49]. According to Uusitalo et al. [49], the input uncertainty of a mechanistic model can be investigated using the single model ensemble method. The single model ensemble performs multiple runs of a model to estimate the variances of the inputs and outputs between repeated model runs and evaluate how the variations in the model outputs can be attributed to the variations in the different input variables [50].

The single model ensemble approach was then used to investigate the degree of uncertainty in the model inputs and to determine how the variations in the model outputs can be attributed to the variations in the different input variables. Ten trials were conducted to track the variations in model input and output parameters over time. The trials were conducted repeatedly between a pair of selected start and end coordinates in the simulated driving environment, namely $S(340.68, 147.55)$ and $E(425.55, 126.33)$. The input variables of our model consist of the current position of the vehicle $P(x, y)$ as well as the road curvature ρ and the adhesion η at the current position of the vehicle, and the output variables are the target coordinate of the vehicle $P_t(x, y)$, the reference speed v_s and the reference looking direction-yaw θ for the movement in the next time step. Specifically, the dynamics of the input variables were captured during the experiments by means of:

- Current position of the vehicle $P(x, y)$: The position $P(x, y)$ was obtained by tracking the physical location of the vehicle in real time in the simulated test environment.
- Road curvature ρ at the current position of the vehicle: The curvature ρ at the current position of the vehicle $P(x, y)$ on the global path was determined in Cartesian space. It was calculated by first fitting a quadratic polynomial to the current position of the vehicle $P(x, y)$ and its neighbouring points, as shown in Fig, 4. The curvature ρ was then a function of the first and second order derivatives of the polynomial using formula (4).
- Road adhesion η at the current position of the vehicle: In the simulated highway driving scene, adhesion η is an inherent property of the road unit. We set up the environment with segmented road sections, where each segment inherited a specific adhesion from its texture and the environmental influence (e.g., 0.08 for ice-covered wet road in Table I). In the experiments, the adhesion η was determined by first identifying the road segment in which the current position of the vehicle $P(x, y)$ occupied and then retrieving the corresponding property from the occupied road segment. In the next step of this research, we would like to use a more intelligent approach for texture recognition and adhesion value recommendation (e.g., the computer vision-based method proposed by Bai et al. [51]), which could help to extend the experimental setup to unknown adhesion contexts.

The results of the analysis of the input uncertainties are presented in Fig. 16. As can be seen in Fig. 16a-16d, the input variables showed different degrees of variations between repeated trials over time. Since formulas (1)-(12) in our model are deterministic computations (i.e., a particular input always produces the same output), the reason for the observed variations is most likely due to the fact that steps 2-6 of our method create a loop that iterates for re-planning at each time step, and the elapsed time of the loops changes slightly at each run. As Choi et al. [52] have pointed out, there is no guarantee that the time between the calling of two commands in a programme is always the same, as the CPUs could be busy with other programmes running in the computer in the meantime. Therefore, the timing for sampling the input variables from the running simulation, which took place at the beginning of each loop, was affected by the change in elapsed time and resulted in the variations visible in the input variables. This uncertainty was then propagated with the model calculations to the output variables and caused the variations in the generated outputs as can be observed in Fig. 16e-16h.

To quantify the variations, the variance was calculated for each input and output variable. As can be seen in Fig. 16a-16b and 16e-16f, the variances of the current and target x, y positions of the vehicle increased significantly from about 230 seconds. A possible explanation for this is that the curvature of the global path started to change from positive to negative at this moment as seen in Fig. 16c, forming a three-point turn driving condition in which the vehicle must turn around to face the opposite direction in a confined space. This requires the vehicle to alternate between acceleration and deceleration, which is reflected in the speed change from approximately 230 seconds shown in Fig. 16h. As the elapsed time of the model loops changes slightly at each run, the time at which the vehicle was captured to enter the three-point turn and encounter the positive-negative curvature change was different between the trials. This led to the observed variations in the vehicle's speed adaptation with respect to curvature between the trials. As speed is the derivative of position with respect to time, significant differences were observed in the positions of the vehicle from about 230 seconds between the trials, which is reflected in the plotted variances. The compatible pattern can also be seen in the variance of the vehicle's reference looking direction θ, which is shown in Fig. 16g. As can also be seen in Fig. 16d, the variance of road adhesion η rises when the road texture changes (e.g., from ice-covered-wetness to asphalt-smooth-wetness), and remains insignificant when the texture stays unchanged. This is because adhesion η is a discrete and not a continuous variable. Although the elapsed time of the model loops changes slightly at each run, the sampled adhesion values η are still the same between the trials as long as the road texture does not differ. If there is no variation, the variance is zero.

Spearman's rank correlation analysis was also performed for the variances of paired input and output variables in a round-robin procedure to assess how the uncertainties in the model outputs can be attributed to the uncertainties in the different inputs. The results are shown in Table V. As can be seen, moderate to strong correlations are identified.

- The uncertainties of the 'target x-coordinate' and 'target y-coordinate' are mostly attributed to the input variables of 'current x-coordinate' ($r = 0.9998$, $p < 0.01$) and 'current y-coordinate' ($r = 0.9993$, $p < 0.01$). An intuitive explanation for this result is that the target coordinate of the vehicle $P_t(x, y)$ is in fact the current position of the vehicle $P(x, y)$ with the preview distance added. Thus, the target coordinate $P_t(x, y)$ correlates mostly with the current position of the vehicle $P(x, y)$, and the uncertainty is synchronised.

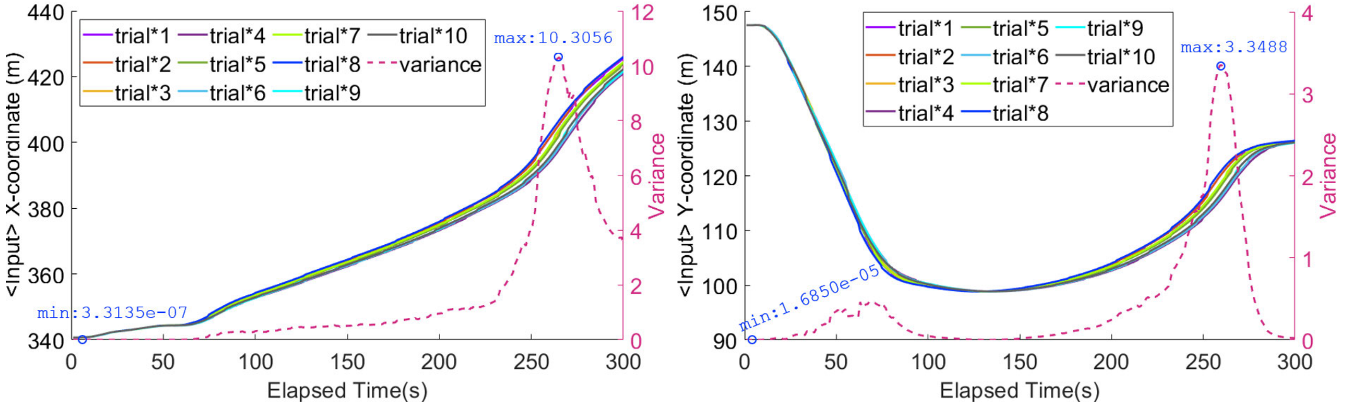

(a) Vehicle's current x-coordinate and variance across 10 trials.

(b) Vehicle's current y-coordinate and variance across 10 trials.

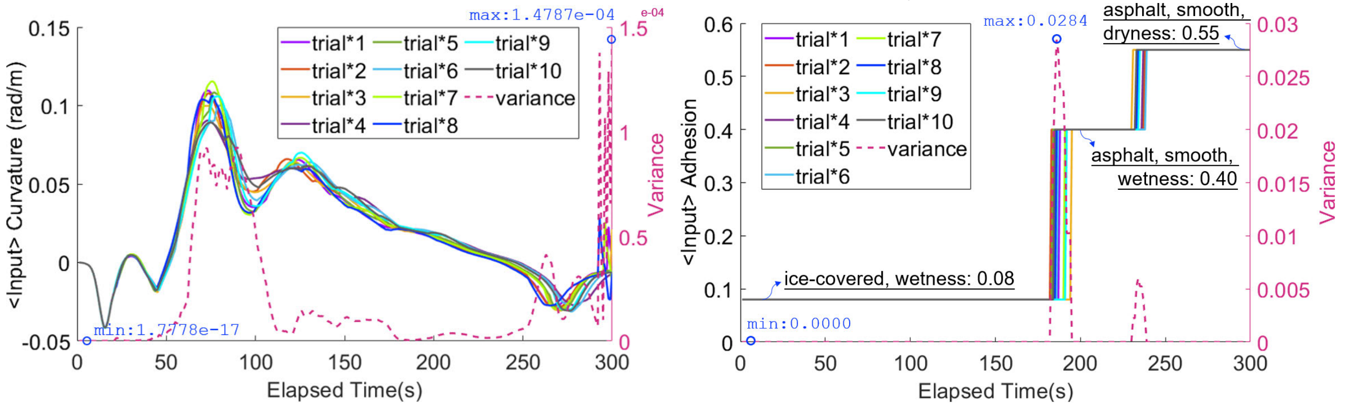

(c) Curvature ρ at vehicle's current position and variance across 10 trials.

(d) Adhesion η at vehicle's current position and variance across 10 trials.

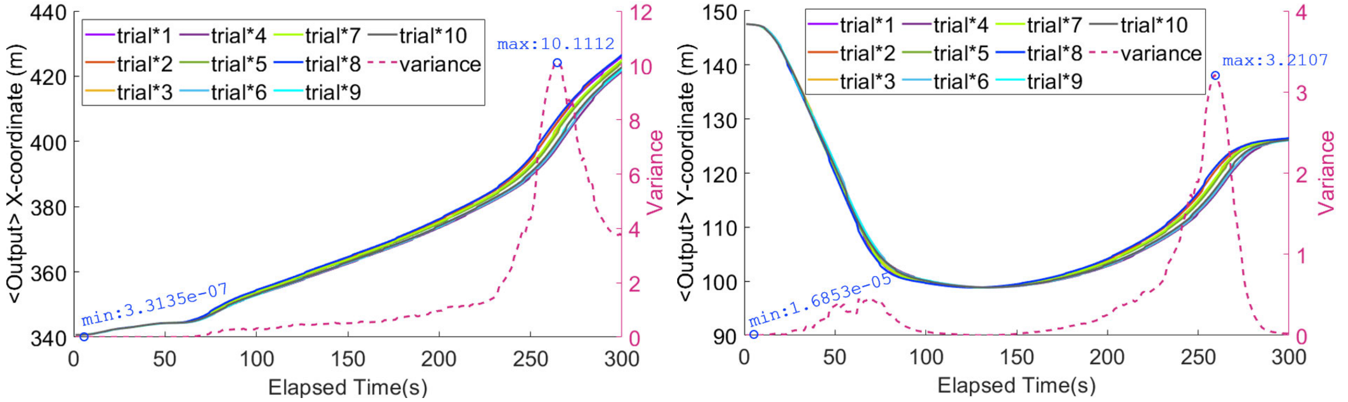

(e) Vehicle's target x-coordinate and variance across 10 trials.

(f) Vehicle's target y-coordinate and variance across 10 trials.

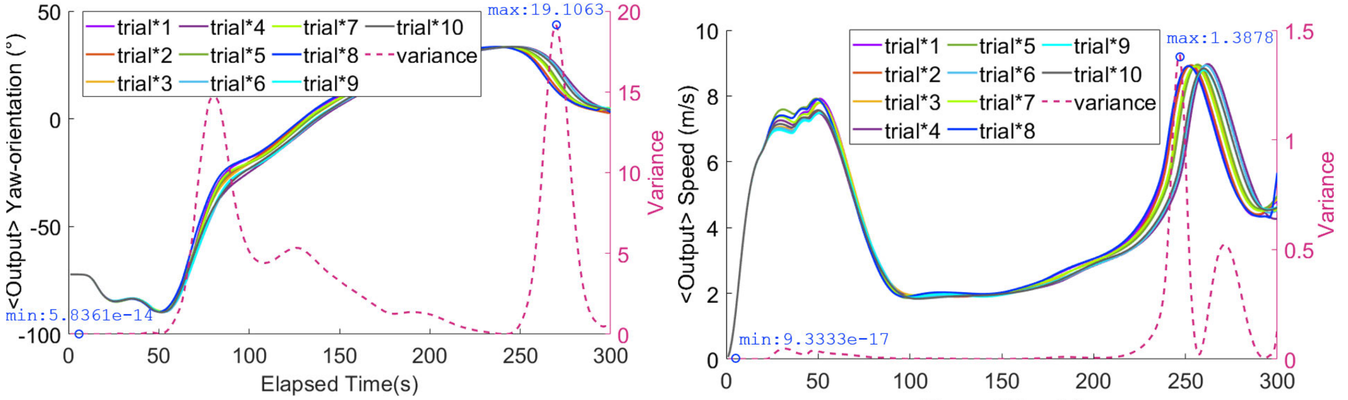

(g) Vehicle's reference looking direction-yaw θ and variance across 10 trials.

(h) Vehicle's reference speed v_s and variance across 10 trials.

Fig. 16. Results of input uncertainty analysis.

TABLE V

SPEARMAN'S RANK CORRELATIONS BETWEEN THE VARIANCES OF THE MODEL INPUT AND OUTPUT VARIABLES

	<output> target x-coordinate	<output> target y-coordinate	<output> reference looking direction	<output> reference speed
<input> current x-coordinate	**$r = 0.9998$, $p < 0.01$**	$r = 0.5016$, $p < 0.01$	$r = 0.2471$, $p < 0.01$	$r = 0.4981$, $p < 0.01$
<input> current y-coordinate	$r = 0.5086$, $p < 0.01$	**$r = 0.9993$, $p < 0.01$**	$r = 0.06180113$, $p > 0.1$	**$r = 0.8381$, $p < 0.01$**
<input> current curvature	$r = 0.2180$, $p < 0.01$	$r = 0.1098$, $0.05 < p < 0.1$	**$r = 0.7982$, $p < 0.01$**	$r = 0.0684$, $p > 0.1$
<input> current adhesion	$r = 0.8283$, $p < 0.01$	$r = 0.5899$, $p < 0.01$	$r = -0.0553$, $p > 0.1$	$r = 0.6341$, $p < 0.01$

Note: The r-value is the indicated correlation between a pair of input and output variables. The p-value is significance level, which examines whether the observed data provide enough evidence against the indicated correlation: $p < 0.01$ strong evidence, $0.01 < p < 0.05$ moderate evidence, $0.05 < p < 0.1$ weak evidence, $p > 0.1$ insufficient evidence.

- The uncertainty of the 'reference looking direction θ' is mostly attributed to the input variable of 'current curvature' ($r = 0.7982$, $p < 0.01$). An intuitive explanation for this result is that curvature describes how much the curve direction changes over a small distance travelled (i.e., angle in rad/m). To safely pass through a curve, the looking direction of the vehicle must make continuous change in accordance with the road curve direction. Thus, the vehicle's reference looking direction θ correlates mostly with the curvature of the road at the vehicle's current position, and the uncertainty is synchronised.
- The uncertainty of the 'reference speed v_s' is mostly attributed to the input variable of 'current y-coordinate' ($r = 0.8381$, $p < 0.01$). A possible explanation for this result is that the road curvature and adhesion, which are used to calculate the reference speed in formula (8), are influenced by the vehicle's current position relative to the global path. Thus, the vehicle's reference speed v_s is shown to correlate mostly with the current position of the vehicle $P(x, y)$, and the uncertainty is synchronised.

IV. CONCLUSION

This paper presents a trajectory planning method for autonomous driving in challenging road conditions. Specifically, the proposed method leverages the complementary effect of road curvature and adhesion on the vehicle speed, and prioritises the trajectory safety through a preview of road constraints (i.e., waypoints, curvature, and adhesion) in a look-ahead distance and the real-time computation of the vehicle speed that satisfies the constraints. This increases the curvature and adhesion adaptability of the planned trajectories. The proposed method also achieves flexible trajectory planning horizon through a module of geometric interpolant, which creates a driving global path by performing a smooth interpolation of the waypoints representation of road network. The reference path provides *a priori* knowledge of lane lines and curves, in which the planning policy can have reference into the future and switch between non-myopic and myopic at a desirable distance. This allows sufficient preview time and increases the safety of planned trajectories.

The proposed method was tested in a simulated driving environment and compared with the state-of-the-art techniques including MPC, DRL and Hybrid A*. In the test, our method outperformed the other techniques and showed good levels of performance in terms of curvature, adhesion adaptability and safety planning. In the next step of this research, we would like to leverage the vehicle's on-board sensors to capture the image of vehicle surroundings and incorporate the computer vision (CV) methods to infer ground or road textures for the recommendation of adhesion values right after (e.g., the algorithm developed by Bai et al. [51]). This could help to extend the practical implementation of our method to unknown adhesion contexts.

REFERENCES

[1] X. Tang, B. Huang, T. Liu, and X. Lin, "Highway decision-making and motion planning for autonomous driving via soft actor-critic," *IEEE Trans. Veh. Technol.*, vol. 71, no. 5, pp. 4706–4717, May 2022, doi: 10.1109/TVT.2022.3151651.

[2] X. Zhao, Y. Ding, Y. Yao, Y. Zhang, C. Bi, and Y. Su, "A multinomial logit model: Safety risk analysis of interchange area based on aggregate driving behavior data," *J. Saf. Res.*, vol. 80, pp. 27–38, Feb. 2022, doi: 10.1016/j.jsr.2021.11.002.

[3] A. Koesdwiady, R. Soua, and F. Karray, "Improving traffic flow prediction with weather information in connected cars: A deep learning approach," *IEEE Trans. Veh. Technol.*, vol. 65, no. 12, pp. 9508–9517, Dec. 2016, doi: 10.1109/TVT.2016.2585575.

[4] Y. Li, J. Jin, T. Chen, L. Han, and Q. Cong, "Effect of an elastic surface on snow and ice accumulation on vehicles," *Cold Regions Sci. Technol.*, vol. 180, Dec. 2020, Art. no. 103154, doi: 10.1016/j.coldregions.2020.103154.

[5] B. Németh and P. Gáspár, "Control design of variable-geometry suspension considering the construction system," *IEEE Trans. Veh. Technol.*, vol. 62, no. 8, pp. 4104–4109, Oct. 2013, doi: 10.1109/TVT.2013.2263156.

[6] X. Du, K. K. K. Htet, and K. K. Tan, "Development of a genetic-algorithm-based nonlinear model predictive control scheme on velocity and steering of autonomous vehicles," *IEEE Trans. Ind. Electron.*, vol. 63, no. 11, pp. 6970–6977, Nov. 2016, doi: 10.1109/TIE.2016.2585079.

[7] D. Hou, L. Zhang, D. Dong, and D. Ou, "Coupling analysis of autonomous vehicles and road safety," in *Proc. Int. Symp. Electr., Electron. Inf. Eng. (ISEEIE)*, Feb. 2022, pp. 57–62, doi: 10.1109/ISEEIE55684.2022.00017.

[8] R. Chai, A. Tsourdos, H. Gao, Y. Xia, and S. Chai, "Dual-loop tube-based robust model predictive attitude tracking control for spacecraft with system constraints and additive disturbances," *IEEE Trans. Ind. Electron.*, vol. 69, no. 4, pp. 4022–4033, Apr. 2022, doi: 10.1109/TIE.2021.3076729.

[9] R. Chai, A. Tsourdos, H. Gao, S. Chai, and Y. Xia, "Attitude tracking control for reentry vehicles using centralised robust model predictive control," *Automatica*, vol. 145, Nov. 2022, Art. no. 110561, doi: 10.1016/j.automatica.2022.110561.

[10] Q. Liu, S. Song, H. Hu, T. Huang, C. Li, and Q. Zhu, "Extended model predictive control scheme for smooth path following of autonomous vehicles," *Frontiers Mech. Eng.*, vol. 17, no. 1, p. 4, Mar. 2022, doi: 10.1007/s11465-021-0660-4.

[11] R. Chai, A. Tsourdos, S. Chai, Y. Xia, A. Savvaris, and C. L. P. Chen, "Multiphase overtaking maneuver planning for autonomous ground vehicles via a desensitized trajectory optimization approach," *IEEE Trans. Ind. Informat.*, vol. 19, no. 1, pp. 74–87, Jan. 2023, doi: 10.1109/TII.2022.3168434.

[12] Z. Cheng, M.-Y. Chow, D. Jung, and J. Jeon, "A big data based deep learning approach for vehicle speed prediction," in *Proc. IEEE 26th Int. Symp. Ind. Electron. (ISIE)*, Jun. 2017, pp. 389–394, doi: 10.1109/ISIE.2017.8001278.

[13] R. Chai, H. Niu, J. Carrasco, F. Arvin, H. Yin, and B. Lennox, "Design and experimental validation of deep reinforcement learning-based fast trajectory planning and control for mobile robot in unknown environment," *IEEE Trans. Neural Netw. Learn. Syst.*, vol. 35, no. 4, pp. 5778–5792, Oct. 2022, doi: 10.1109/TNNLS.2022.3209154.

[14] R. Chai, A. Tsourdos, A. Savvaris, S. Chai, Y. Xia, and C. L. P. Chen, "Design and implementation of deep neural network-based control for automatic parking maneuver process," *IEEE Trans. Neural Netw. Learn. Syst.*, vol. 33, no. 4, pp. 1400–1413, Apr. 2022, doi: 10.1109/TNNLS.2020.3042120.

[15] R. Chai, D. Liu, T. Liu, A. Tsourdos, Y. Xia, and S. Chai, "Deep learning-based trajectory planning and control for autonomous ground vehicle parking maneuver," *IEEE Trans. Autom. Sci. Eng.*, vol. 20, no. 3, pp. 1633–1647, Jul. 2023, doi: 10.1109/TASE.2022.3183610.

[16] J. Pan, J. Wang, and S. Xing, "Dynamic trajectory planning and optimization for automated driving on ice and snow covered road," *IEEE Access*, vol. 11, pp. 36365–36378, 2023, doi: 10.1109/ACCESS.2023.3266006.

[17] Z. Fu, L. Xiong, Z. Qian, B. Leng, D. Zeng, and Y. Huang, "Model predictive trajectory optimization and tracking in highly constrained environments," *Int. J. Automot. Technol.*, vol. 23, no. 4, pp. 927–938, Aug. 2022, doi: 10.1007/s12239-022-0081-3.

[18] H. Li, G. Yu, B. Zhou, P. Chen, Y. Liao, and D. Li, "Semantic-level maneuver sampling and trajectory planning for on-road autonomous driving in dynamic scenarios," *IEEE Trans. Veh. Technol.*, vol. 70, no. 2, pp. 1122–1134, Feb. 2021, doi: 10.1109/TVT.2021.3051178.

[19] V. Trentin, A. Artuñedo, J. Godoy, and J. Villagra, "Multi-modal interaction-aware motion prediction at unsignalized intersections," *IEEE Trans. Intell. Vehicles*, vol. 8, no. 5, pp. 3349–3365, Mar. 2023, doi: 10.1109/TIV.2023.3254657.

[20] L. Zhai, C. Wang, Y. Hou, and C. Liu, "MPC-based integrated control of trajectory tracking and handling stability for intelligent driving vehicle driven by four hub motor," *IEEE Trans. Veh. Technol.*, vol. 71, no. 3, pp. 2668–2680, Mar. 2022, doi: 10.1109/TVT.2022.3140240.

[21] X. Li, X. Gao, W. Zhang, and L. Hao, "Smooth and collision-free trajectory generation in cluttered environments using cubic B-spline form," *Mechanism Mach. Theory*, vol. 169, Mar. 2022, Art. no. 104606, doi: 10.1016/j.mechmachtheory.2021.104606.

[22] I. L. Jover, T. Debarre, S. Aziznejad, and M. Unser, "Coupled splines for sparse curve fitting," *IEEE Trans. Image Process.*, vol. 31, pp. 4707–4718, 2022, doi: 10.1109/TIP.2022.3187286.

[23] H. Zong, H. Liu, Q. Ma, Y. Tian, M. Zhou, and M. Y. Wang, "VCUT level set method for topology optimization of functionally graded cellular structures," *Comput. Methods Appl. Mech. Eng.*, vol. 354, pp. 487–505, Sep. 2019, doi: 10.1016/j.cma.2019.05.029.

[24] S. Havemann, J. Edelsbrunner, P. Wagner, and D. Fellner, "Curvature-controlled curve editing using piecewise clothoid curves," *Comput. Graph.*, vol. 37, no. 6, pp. 764–773, Oct. 2013, doi: 10.1016/j.cag.2013.05.017.

[25] W. Fan, C.-H. Lee, and J.-H. Chen, "A realtime curvature-smooth interpolation scheme and motion planning for CNC machining of short line segments," *Int. J. Mach. Tools Manuf.*, vol. 96, pp. 27–46, Sep. 2015, doi: 10.1016/j.ijmachtools.2015.04.009.

[26] M. S. Dashti, M. RezaZadeh, M. Khanzadi, and H. Taghaddos, "Integrated BIM-based simulation for automated time-space conflict management in construction projects," *Autom. Construction*, vol. 132, Dec. 2021, Art. no. 103957, doi: 10.1016/j.autcon.2021.103957.

[27] B. Leng, D. Jin, X. Hou, C. Tian, L. Xiong, and Z. Yu, "Tire-road peak adhesion coefficient estimation method based on fusion of vehicle dynamics and machine vision," *IEEE Trans. Intell. Transp. Syst.*, vol. 23, no. 11, pp. 21740–21752, Nov. 2022, doi: 10.1109/TITS.2022.3183691.

[28] J. Pi et al., "Implementation of effective scale factor matching and axial centripetal error compensation for a rotating accelerometer gravity gradiometer," *IEEE Trans. Instrum. Meas.*, vol. 72, pp. 1–11, 2023, doi: 10.1109/TIM.2023.3235419.

[29] G. Ali, S. McLaughlin, and M. Ahmadian, "Quantifying the effect of roadway, driver, vehicle, and location characteristics on the frequency of longitudinal and lateral accelerations," *Accident Anal. Prevention*, vol. 161, Oct. 2021, Art. no. 106356, doi: 10.1016/j.aap.2021.106356.

[30] Z. Zhou, J. Zhao, Z. Zhang, and X. Li, "Motion planning of dual-chain manipulator based on artificial bee colony algorithm," in *Proc. 9th Int. Conf. Control, Autom. Robot. (ICCAR)*, Apr. 2023, pp. 55–60, doi: 10.1109/ICCAR57134.2023.10151753.

[31] D. Cerruti and M. Filippini, "Speed limits and vehicle accidents in built-up areas: The impact of 30 km/h zones," ETH Zurich, Center Econ. Res. (CER-ETH), Zurich, Switzerland, Econ. Work. Paper 21/356, 2021, doi: 10.3929/ethz-b-000490316.

[32] M. E. Dean, N. Lubbe, R. Fredriksson, S. Sternlund, and H. C. Gabler, "Assessing the applicability of impact speed injury risk curves based on U.S. data to defining safe speeds in the U.S. and Sweden," *Accident Anal. Prevention*, vol. 190, Sep. 2023, Art. no. 107151, doi: 10.1016/j.aap.2023.107151.

[33] C. Fu and H. Liu, "Investigating distance halo effect of fixed automated speed camera based on taxi GPS trajectory data," (English Edition), *J. Traffic Transp. Eng.*, vol. 10, no. 1, pp. 70–85, Feb. 2023, doi: 10.1016/j.jtte.2021.05.005.

[34] J. Li, H. Qin, J. Wang, and J. Li, "OpenStreetMap-based autonomous navigation for the four wheel-legged robot via 3D-LiDAR and CCD camera," *IEEE Trans. Ind. Electron.*, vol. 69, no. 3, pp. 2708–2717, Mar. 2022, doi: 10.1109/TIE.2021.3070508.

[35] B. Zhang, J. He, and D. Pei, "Global trajectory optimization of mobile robot based on minimum snap," in *Proc. IEEE 6th Inf. Technol. Mechatronics Eng. Conf. (ITOEC)*, vol. 6, Mar. 2022, pp. 36–41, doi: 10.1109/ITOEC53115.2022.9734396.

[36] A. Sharma, Z. Zheng, and A. Bhaskar, "Is more always better? The impact of vehicular trajectory completeness on car-following model calibration and validation," *Transp. Res. B, Methodol.*, vol. 120, pp. 49–75, Feb. 2019, doi: 10.1016/j.trb.2018.12.016. [Online]. Available: https://www.sciencedirect.com/science/article/pii/S0191261518301528

[37] Z. Yu, J. Hu, G. Min, Z. Zhao, W. Miao, and M. S. Hossain, "Mobility-aware proactive edge caching for connected vehicles using federated learning," *IEEE Trans. Intell. Transp. Syst.*, vol. 22, no. 8, pp. 5341–5351, Aug. 2021, doi: 10.1109/TITS.2020.3017474.

[38] C. Lyu, X. Wu, Y. Liu, and Z. Liu, "A partial-Fréchet-distance-based framework for bus route identification," *IEEE Trans. Intell. Transp. Syst.*, vol. 23, no. 7, pp. 9275–9280, Jul. 2022, doi: 10.1109/TITS.2021.3069630.

[39] E. E. Sigmund et al., "Diffusion-based MR methods for bone structure and evolution," *Magn. Reson. Med.*, vol. 59, no. 1, pp. 28–39, Jan. 2008, doi: 10.1002/mrm.21281.

[40] X. Du, N. Wang, Y. Pei, J. Zhang, and A. Wang, "The influence of the centroid of loaded goods under the ice and snow road on the handling stability of articulated semi-trailer truck," in *Proc. 6th Int. Conf. Transp. Inf. Saf. (ICTIS)*, Oct. 2021, pp. 483–489, doi: 10.1109/ICTIS54573.2021.9798413.

[41] S. T. Radev, M. D'Alessandro, U. K. Mertens, A. Voss, U. Köthe, and P.-C. Bürkner, "Amortized Bayesian model comparison with evidential deep learning," *IEEE Trans. Neural Netw. Learn. Syst.*, vol. 34, no. 8, pp. 4903–4917, Aug. 2023, doi: 10.1109/TNNLS.2021.3124052.

[42] B. Lambert, F. Forbes, S. Doyle, H. Dehaene, and M. Dojat, "Trustworthy clinical AI solutions: A unified review of uncertainty quantification in deep learning models for medical image analysis," *Artif. Intell. Med.*, vol. 150, Apr. 2024, Art. no. 102830, doi: 10.1016/j.artmed.2024.102830.

[43] W. Tai, X. Li, J. Zhou, and S. Arik, "Asynchronous dissipative stabilization for stochastic Markov-switching neural networks with completely- and incompletely-known transition rates," *Neural Netw.*, vol. 161, pp. 55–64, Apr. 2023, doi: 10.1016/j.neunet.2023.01.039.

[44] S. Bi, M. Beer, S. Cogan, and J. Mottershead, "Stochastic model updating with uncertainty quantification: An overview and tutorial," *Mech. Syst. Signal Process.*, vol. 204, Dec. 2023, Art. no. 110784, doi: 10.1016/j.ymssp.2023.110784.

[45] S. Munikoti, D. Agarwal, L. Das, and B. Natarajan, "A general framework for quantifying aleatoric and epistemic uncertainty in graph neural networks," *Neurocomputing*, vol. 521, pp. 1–10, Feb. 2023, doi: 10.1016/j.neucom.2022.11.049. [Online]. Available: https://www.sciencedirect.com/science/article/pii/S0925231222014424

[46] L. Cao, H. Zhang, Z. Meng, and X. Wang, "A parallel GRU with dual-stage attention mechanism model integrating uncertainty quantification for probabilistic RUL prediction of wind turbine bearings," *Rel. Eng. Syst. Saf.*, vol. 235, Jul. 2023, Art. no. 109197, doi: 10.1016/j.ress.2023.109197.

[47] M. Farrokhifar, Y. Nie, and D. Pozo, "Energy systems planning: A survey on models for integrated power and natural gas networks coordination," *Appl. Energy*, vol. 262, Mar. 2020, Art. no. 114567, doi: 10.1016/j.apenergy.2020.114567.

[48] R. Chapagain et al., "Decomposing crop model uncertainty: A systematic review," *Field Crops Res.*, vol. 279, Apr. 2022, Art. no. 108448, doi: 10.1016/j.fcr.2022.108448.

[49] L. Uusitalo, A. Lehikoinen, I. Helle, and K. Myrberg, "An overview of methods to evaluate uncertainty of deterministic models in decision support," *Environ. Model. Softw.*, vol. 63, pp. 24–31, Jan. 2015, doi: 10.1016/j.envsoft.2014.09.017.

[50] Z. Zheng, L. Zhao, and K. W. Oleson, "Large model structural uncertainty in global projections of urban heat waves," *Nature Commun.*, vol. 12, no. 1, p. 3736, Jun. 2021, doi: 10.1038/s41467-021-24113-9.

[51] N. Bai et al., "A robotic sensory system with high spatiotemporal resolution for texture recognition," *Nature Commun.*, vol. 14, no. 1, p. 7121, Nov. 2023, doi: 10.1038/s41467-023-42722-4.

[52] H. Choi, Y. Xiang, and H. Kim, "PiCAS: New design of priority-driven chain-aware scheduling for ROS2," in *Proc. IEEE 27th Real-Time Embedded Technol. Appl. Symp. (RTAS)*, May 2021, pp. 251–263, doi: 10.1109/RTAS52030.2021.00028.

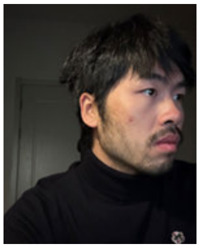

Yifan Gao received the Bachelor of Engineering (B.Eng.) degree from Chongqing University and the Doctor of Philosophy (Ph.D.) degree from The University of Auckland. He was a Post-Doctoral Fellow with Zhejiang University. In 2023, he joined the Research Center for Frontier Fundamental Studies, Zhejiang Lab, participating in an autonomous drive research project to develop trajectory planning algorithms for unstructured road conditions. His research interests include trajectory planning, driving simulation generation, and human–computer interaction.

Wei Li received the bachelor's and Ph.D. degrees from Tsinghua University in 2014 and 2019, respectively. She is currently an Associate Professor with the Institute of Computing Technology, Chinese Academy of Sciences. Her research interests include multi-sensor fusion, satellite positioning, SLAM, and motion planning, with a special focus on autonomous navigation.

Yu Hu (Member, IEEE) received the B.S., M.S., and Ph.D. degrees in electrical engineering from the University of Electronic Science and Technology of China (UESTC), Chengdu, China, in 1997, 1999, and 2003, respectively. She is currently a Professor with the Institute of Computing Technology (ICT), Chinese Academy of Sciences (CAS), Beijing, China. Her research interests include autonomous driving, deep learning, and algorithm acceleration. She is a Senior Member of China Computer Federation (CCF).